Numerical Study of Quantum Spin Models by Loop Algorithm(Dissertation_全文)

AUTHOR(S):

Harada, Kenji

CITATION:

Harada, Kenji. Numerical Study of Quantum Spin Models by Loop Algorithm. 京都大学, 1998, 博士(工学)

ISSUE DATE:

1998-05-25

URL:

https://doi.org/10.11501/3138605

Numerical Study of Quantum Spin Models by Loop Algorithm

Kenji Harada

March 1998

Numerical Study of Quantum Spin Models by Loop Algorithm

Kenji Harada

March 1998

Preface

Various models in condensed matter and quantum field theories have a large degree of freedom. In the progress of efficiency of computers, direct computational methods for those models become one of powerful tools for researchers. The following three methods are important: Monte Carlo method, molecular dynamical method and exact calculation method. The last method needs the order of computational times as the exponential of degree of freedom, while the formers do only a polynomial order of degree of freedom and a correlation time. If the correlation time were small, we could carry out the calculation. In the present thesis, we use Monte Carlo method only.

In general, the correlation time is a natural way to become large in conventional Monte Carlo methods. For Ising model, it increases in proportions to about the square of linear dimension of system near a critical point. This phenomena is called critical slowing down. This makes Monte Carlo simulation for large systems difficult.

To overcome the difficulty, many people have proposed various new algorithms of Monte Carlo methods. In 1987, Swendsen and Wang (SW) [40] invented a new algorithm called cluster algorithm for classical Potts model. It is reported to have no critical slowing down. It has been extended to other models. It must be noted that Evertz *et al.* [14] applied it to quantum spin models in 1993. The new version of algorithms for quantum spin models is called loop algorithm. They have some excellent features which may lead to successful solution, and yet they have been applied only to a few models.

Loop algorithms drastically reduce critical slowing down and are naturally ergotic in contrast with conventional worldline Monte Carlo methods. They can be directly implemented on continuous imaginary time without any systematic error of Suzuki–Trotter decomposition, and allow some improved estimators for various quantities. Moreover they can be generalized for various quantum spin models with higher spins values.

In the present thesis, the loop algorithm is used to study the phase transition of spin-1/2 quantum XY model and the property of spin-1 Heisenberg antiferromagnet in low temperatures. Their simulations can be done above-mentioned features of loop algorithms. Many computations are carried out to see.

Chapter 1 reviews loop algorithms on discrete and continuous imaginary time and discusses improved estimators. The general proof of efficiency of improved estimators is also given. Chapter 2 investigates the two-dimensional spin-1/2 XY

model through loop algorithms near and below the critical temperature and discusses the phase transition. Chapter 3 reports results of extensive Monte Carlo simulations of the two-dimensional spin-1 square lattice quantum Heisenberg antiferromagnet by a loop algorithm on continuous imaginary time. Those results are compared with theoretical predictions and experimental measurements.

Acknowledgment

I would like to thank Prof. T. Munakata and Prof. M. Funakoshi for useful suggestions and Prof. T. Nogi for helpful discussions. I am grateful to Prof. N. Kawashima and Prof. M. Troyer for our collaboration. I wish to thank Prof. A. Cuccoli, Prof. V. Tognetti, Prof. R. Vaia and Prof. P. Verrucchi for providing the results of their PQSCHA theory and to Prof. K. Nakajima for the experimental data on La_2NiO_4. Finally, I am grateful to my parents for their understanding and encouragement.

The calculations in the present thesis were performed on the Fujitsu VPP500 at Kyoto University Data Processing Center and at ISSP, the university of Tokyo and on the Hitachi SR2201 massively parallel computer at the computer center of the University of Tokyo.

Kyoto, Kenji Harada
March 1998

Contents

List of Tables

List of Figures

1. Loop algorithm for quantum Monte Carlo simulation

1.1 Introduction

Quantum Monte Carlo method [39] is one of powerful methods to solve various problems of quantum models. It is well known that the traditional implementation of quantum Monte Carlo method has some difficulties: critical slowing down, ergodicity, systematic error and negative-sign problem.

In order to overcome them, various new algorithms have been proposed. One of them, is the so called loop algorithm, proposed by Evertz *et al.* [14] in 1993. It has some excellent features which may lead to successful solution.

In this chapter, we will introduce loop algorithm and give an improved estimator for quantum Monte Carlo simulation, and analyze their performance. Before going into the detail, we will survey a general approach used in quantum Monte Carlo simulation (§1.2) and a traditional worldline algorithm (§1.3). Section 1.4 reviews the loop algorithm by Kandel–Domany framework [20, 23] and Sec. 1.5 treats the improved estimator and its performance.

1.2 Quantum Monte Carlo method

In quantum statistical mechanics we often ought to calculate the expectation of a observable $\hat{X}$ in the form

$$\langle \hat{X} \rangle \equiv \frac{\mathrm{Tr} \hat{X} e^{-\beta \hat{H}}}{\mathrm{Tr} e^{-\beta \hat{H}}}, \tag{1.1}$$

where $\hat{H}$ is a Hamiltonian, β is inverse temperature $1/k_{\mathrm{B}}T$. In order to calculate $e^{-\beta \hat{H}}$ in eq. (1.1), which is called density matrix, we have to diagonalize the Hamiltonian. But it is practically impossible to diagonalize except few special cases. The main reason is that the Hamiltonian is usually a sum of uncommutative operators. So we need to approximate the density matrix $e^{-\beta \hat{H}}$ appropriately.

Since the density matrix $e^{-\beta \hat{H}}$ can be considered a time evolution operator of Schrödinger equation with the imaginary time $t = i\hbar\beta$, it is called propagator and can be represented with Feynman path integral as follows.

Take an n-th order approximant $f_n(x)$ of the exponential operator $e^{-x\hat{H}}$:

$$e^{-x\hat{H}} = f_n(x) + O(x^{n+1}). \tag{1.2}$$

The density matrix is then approximated as

$$e^{-\beta\hat{H}} = \left(e^{-(\beta/m)\hat{H}}\right)^m \approx (f_n(\beta/m))^m + O(\beta^{n+1}/m^n). \tag{1.3}$$

A simple approximant is

$$e^{-x\hat{H}} = 1 - x\hat{H} + O(x^2). \tag{1.4}$$

However, it is not unitary and hence not applicable for quantum Monte Carlo simulations. We usually use another approximant called Suzuki–Trotter (ST) decomposition instead:

$$e^{-x\hat{H}} = \prod_i e^{-x\hat{H}_i} + O(x^2), \tag{1.5}$$

where $\hat{H} = \sum_i \hat{H}_i$, each addend Hamiltonian $\hat{H}_i$ being easily diagonalizable. The approximant is unitary.

Using ST decomposition, we calculate the density matrix as

$$\begin{aligned} e^{-\beta\hat{H}} &\approx \left(\prod_{i=1}^{l} e^{-(\beta/m)\hat{H}_i}\right)^m & (1.6)\\ &= \sum_{C_2,\cdots,C_{lm}} e^{-(\beta/m)\hat{H}_1}|C_2\rangle\langle C_2|e^{-(\beta/m)\hat{H}_2}|C_3\rangle\langle C_3|\cdots \\ &\qquad \cdots|C_{lm}\rangle\langle C_{lm}|e^{-(\beta/m)\hat{H}_l}, & (1.7) \end{aligned}$$

where $|C_i\rangle$ totally form a complete set of states. This approximant converges to the original density matrix in the limit $m \to \infty$. The limit is not but the Feynman path integral of the time evolution operator of Schrödinger equation along the imaginary time axis. Hence eq. (1.7) may be said to be an approximation of Feynman path integral with discrete imaginary time.

Since each exponential operator $e^{-(\beta/m)\hat{H}_i}$ is also diagonalizable, it can be taken as one of local Boltzmann factors of a classical system. Consequently, we can apply Monte Carlo methods for classical models to calculate the density matrix of quantum models.

Note that a d-dimensional quantum model corresponds to a $(d+1)$-dimensional classical system. The index i of $|C_i\rangle$ plays a role of an auxiliary dimension. It is the imaginary time in Feynman path integral language. In quantum Monte Carlo methods, it is called Trotter direction.

1.3 Worldline algorithm

The worldline algorithm [39] is traditionally used to perform Monte Carlo simulation for quantum models. It lives on a worldline representation.

In Sec. 1.3.1, we describe what worldline representation is. In Sec. 1.3.2, we explain traditional worldline algorithms. In Sec. 1.3.3, we survey their difficulties in computation.

1.3.1 Worldline representation

In general, when a d-dimensional quantum Hamiltonian comprises short-range interactions, it can be replaced by a $(d+1)$-dimensional classical system with short-range interactions. Using ST decomposition, we put the partition function Z as

$$Z \approx \sum_S \prod_p w_p(S_p), \tag{1.8}$$

where S_p is a set of classical spins belonging to plaquette p on the $(d+1)$-dimensional lattice and summation $\sum_S$ extends over all configurations of spins on $(d+1)$-dimensional lattice sites. In the following, we introduce an example of an $S = 1/2$ quantum XXZ model on a one-dimensional chain.

One-dimensional $S = 1/2$ quantum XXZ model

The $S = 1/2$ quantum XXZ model on a one-dimensional chain of N sites is defined by the following Hamiltonian:

$$\hat{H} = -\sum_{i=1}^{N} \left[J_x(\hat{S}_i^x \hat{S}_{i+1}^x + \hat{S}_i^y \hat{S}_{i+1}^y) + J_z \hat{S}_i^z \hat{S}_{i+1}^z + B\hat{S}_i^z \right], \tag{1.9}$$

where $\hat{S}_i^\mu$ is quantum spin-1/2 operator at each site i ($\mu = x, y, z$). For the periodic boundary condition the $(N+1)$-site is identified with the 1-site.

The Hamiltonian can be considered as a sum of two uncommutative: $\hat{H} = \hat{H}_{odd} + \hat{H}_{even}$. $\hat{H}_{odd,even}$ is equal to $\sum_{i:\text{odd,even}} \hat{H}_i$, where $\hat{H}_i$ is defined as

$$\hat{H}_i = -J_x(\hat{S}_i^x \hat{S}_{i+1}^x + \hat{S}_i^y \hat{S}_{i+1}^y) - J_z \hat{S}_i^z \hat{S}_{i+1}^z - \frac{B}{2}(\hat{S}_i^z + \hat{S}_{i+1}^z). \tag{1.10}$$

Using ST decomposition in a small interval $\Delta\tau$,

$$e^{-\Delta\tau \hat{H}} \approx e^{-\Delta\tau \hat{H}_{odd}} e^{-\Delta\tau \hat{H}_{even}} + O(\Delta\tau^2), \tag{1.11}$$

we can get the desired factorization of the partition function as

$$\begin{aligned} Z &\equiv \mathrm{Tr} e^{-\beta\hat{H}} && (1.12)\\ &= \mathrm{Tr}(e^{-(\beta/m)\hat{H}})^m && (1.13)\\ &= \mathrm{Tr}\left(e^{-(\beta/m)\hat{H}_{odd}} e^{-(\beta/m)\hat{H}_{even}}\right)^m + O((\beta/m)^2), && (1.14) \end{aligned}$$

where m is called Trotter number.

We calculate eq. (1.14) as follows:

$$\begin{aligned} Z \approx \sum_{C_1,\cdots,C_{2m}} & \langle C_1|e^{-(\beta/m)\hat{H}_{odd}}|C_2\rangle\langle C_2|e^{-(\beta/m)\hat{H}_{even}}|C_3\rangle \\ & \cdots \langle C_{2m}|e^{-(\beta/m)\hat{H}_{even}}|C_1\rangle, \end{aligned} \tag{1.15}$$

where $\{|C_t\rangle\}$ is a complete set of states. Here $|C_t\rangle$ is a direct product of eigenstates of $\hat{S}_i^z$ on a one-dimensional chain:

$$|C_t\rangle \equiv \left|S_{1,t}^z\right\rangle \left|S_{2,t}^z\right\rangle \cdots \left|S_{N,t}^z\right\rangle, \tag{1.16}$$

where $\hat{S}_i^z \left|S_{i,t}^z\right\rangle = S_{i,t}^z \left|S_{i,t}^z\right\rangle$ with $S_{i,t}^z = \pm\frac{1}{2}$.

Since each $\hat{H}_{odd,even}$ itself contains only commutative terms, it is further decomposed into the product of two-spin propagators:

$$\langle C_t|e^{-(\beta/m)\hat{H}_{odd,even}}|C_{t+1}\rangle = \langle C_t| \prod_{i:\text{odd,even}} e^{-(\beta/m)\hat{H}_i}|C_{t+1}\rangle. \tag{1.17}$$

For simplicity, we denote each two-spin propagator by

$$w(S_p) \equiv \langle C_t|\, e^{-(\beta/m)\hat{H}_i}\, |C_{t+1}\rangle\,, \tag{1.18}$$

where p stands for a plaquette that consists of four classical spins (see Fig. 1.1),

$$p \equiv ((i,t),(i+1,t),(i,t+1),(i+1,t+1)) \tag{1.19}$$

and S_p is the local spin configuration defined as

$$S_p \equiv (S_{i,t}^z, S_{i+1,t}^z, S_{i,t+1}^z, S_{i+1,t+1}^z). \tag{1.20}$$

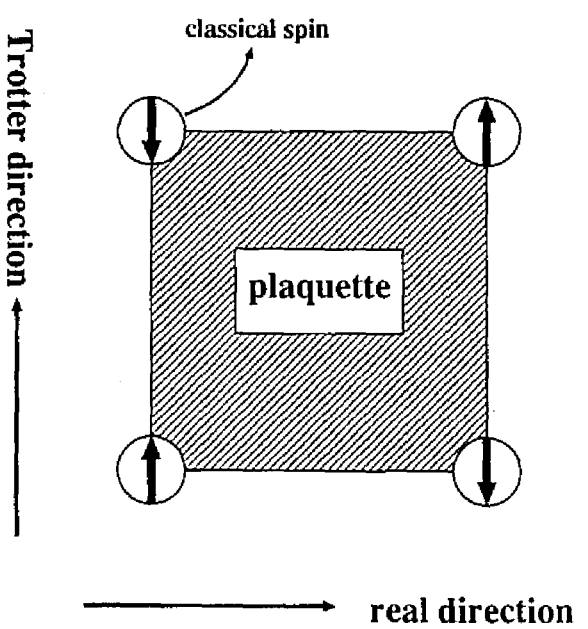

Figure 1.1: A plaquette consists of four classical spins.

We denote the four states of spin pairs by $1 = \uparrow\uparrow$, $2 = \uparrow\downarrow$, $3 = \downarrow\uparrow$ and $4 = \downarrow\downarrow$. The two-spin propagator can be written explicitly as

$$\begin{pmatrix} e^{\frac{\beta}{4m}J_z} e^{\frac{\beta}{2m}B} & 0 & 0 & 0 \\ 0 & e^{-\frac{\beta}{4m}J_z}\cosh(\frac{\beta}{2m}J_x) & e^{-\frac{\beta}{4m}J_z}\sinh(\frac{\beta}{2m}J_x) & 0 \\ 0 & e^{-\frac{\beta}{4m}J_z}\sinh(\frac{\beta}{2m}J_x) & e^{-\frac{\beta}{4m}J_z}\cosh(\frac{\beta}{2m}J_x) & 0 \\ 0 & 0 & 0 & e^{\frac{\beta}{4m}J_z} e^{-\frac{\beta}{2m}B} \end{pmatrix}. \quad (1.21)$$

In the above 4×4 matrix representation of eq. (1.21), the column index corresponds to four possible initial state $\left|S^z_{i,t}, S^z_{i+1,t}\right\rangle$, and the row index $\left|S^z_{i,t+1}, S^z_{i+1,t+1}\right\rangle$.

Consequently, we replace the partition function as follows:

$$Z \approx \sum_{S^z_{i,t}} \prod_p w(S_p), \quad (1.22)$$

where summation $\sum_{S^z_{i,t}}$ extends over all configurations of spins $S^z_{i,t}$ on a $(1+1)$-dimensional lattice and product $\prod_p$ extends over all shaded plaquette on lattice (see Fig. 1.2). The one-dimensional $S = 1/2$ quantum XXZ model is approximated by the $(1+1)$-dimensional classical Ising model with four spin plaquette interactions.

From the following conservation rule,

$$S^z_{i,t} + S^z_{i+1,t} = S^z_{i,t+1} + S^z_{i+1,t+1} \qquad \text{on each plaquette,} \quad (1.23)$$

we can draw lines connecting the corresponding up spins in the Trotter direction (see Fig. 1.3). This line is called worldline. Since each spin configuration corresponds to each worldline configuration one by one, we can describe system by using worldlines.

1.3.2 Worldline algorithm

A traditional Monte Carlo algorithm is a sequence of local updates of system configuration. In classical systems, Metropolis method or heat-bath method is often used, which usually updates a single spin at a time. In quantum systems, worldline algorithm is used instead, which updates local worldline configurations. The procedure consists of two steps:

(i) Proposing local deformations of a worldline configuration.

(ii) Accepting or rejecting them with a suitable probability rule.

Various local deformations are taken for several kinds of quantum models. We only show an example of one-dimensional $S = 1/2$ quantum XXZ model in the following.

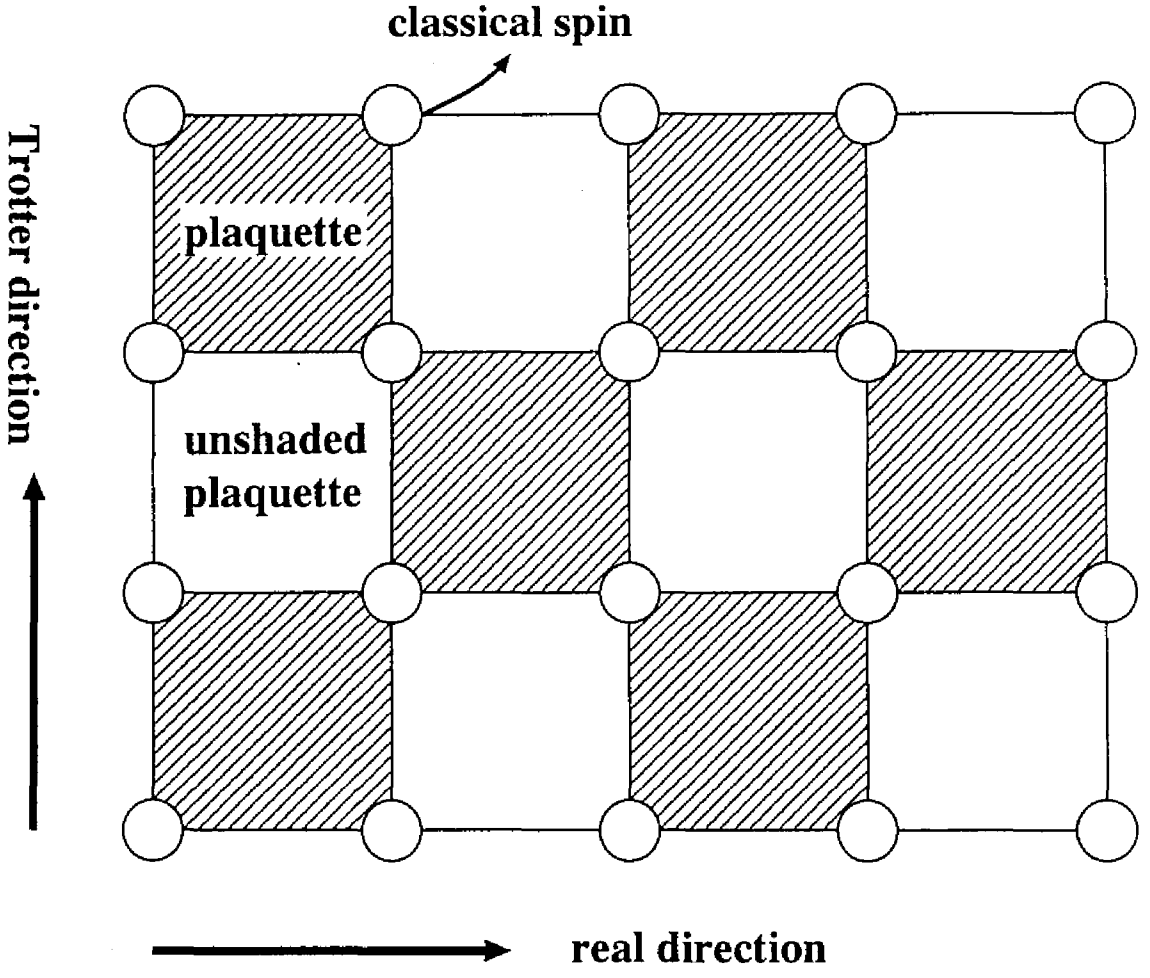

Figure 1.2: A checker-board square lattice.

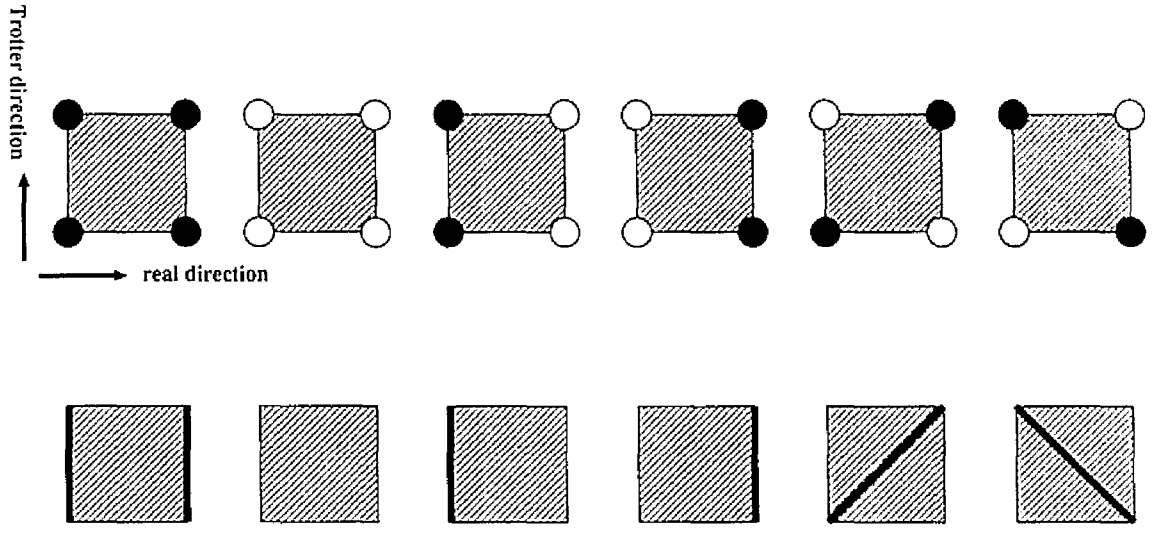

Figure 1.3: Allowed spin configurations, which have non-zero Boltzmann weight, and their worldline representations. A top row represents allowed spin configurations. Black and white circles show up and down classical spins, respectively. A bottom row represents corresponding worldline configurations. Black thick lines are worldlines.

Worldline algorithm for one-dimensional $S = 1/2$ quantum XXZ model

Using ST decomposition with a fixed Trotter number m, we can derive the $(1+1)$-dimensional classical system as eq. (1.22) from the one-dimensional $S = 1/2$ quantum XXZ model (see Sec. 1.3.1).

Allowed spin configurations which have non-zero Boltzmann weight keep the conservation rule eq. (1.23). A local deformation also must keep it. A simplest one is a flipping of spins which belong to an unshaded plaquette in Fig. 1.2. It corresponds to a local move of worldline (see Fig. 1.4 (a)).

In order to keep the detailed balance condition (see Appendix A), the proposed local deformation is accepted with the following probability (heat-bath method):

$$\frac{w(S'_{p1})w(S'_{p2})w(S'_{p3})w(S'_{p4})}{w(S_{p1})w(S_{p2})w(S_{p3})w(S_{p4}) + w(S'_{p1})w(S'_{p2})w(S'_{p3})w(S'_{p4})}, \tag{1.24}$$

where S'_μ, $\mu = (p1, p2, p3, p4)$ is proposed spin configuration (see Fig. 1.4 (a)) and $w(S_p)$ is the two-spin propagator defined in eq. (1.18).

But these local updates cannot afford to create another configurations which may have a different magnetization and winding number. So we need global updates. Usually, two ways of global updates are used:

- Flipping all spins with a same value on a line along Trotter direction (Fig. 1.4 (b)).

- Flipping all spins with alternating values on a line along real direction (Fig. 1.4 (c)).

Each probability for accepting is calculated from the detailed balance condition.

1.3.3 Difficult Points

The traditional worldline algorithm has many difficulties:

- Increasing autocorrelation between successive Monte Carlo configurations near to a critical point or low temperatures.
- Systematic error due to ST decomposition.
- Ergodicity.
- Negative-sign problem.

The loop algorithm almost overcomes these difficulties except the last problem. We discuss them in the following.

Autocorrelation

A local update algorithm, such as worldline algorithm, for Monte Carlo simulations near to a critical point of a physical model generally meets with extremely large autocorrelation between successive Monte Carlo configurations. The phenomenon is related to critical slowing down in real materials.

In Monte Carlo simulations, the statistical error $\Delta(A)$ of an observed quantity A is related to the variance of the estimator $\mathcal{O}$, the sampling number N_{sample} and the autocorrelation time τ:

$$\Delta(A) \approx \sqrt{\frac{\mathrm{Var}(\mathcal{O})}{(N_{\text{sample}}/2\tau)}}. \tag{1.25}$$

It demands such a large sampling number as compared with the autocorrelation time to assure a small error.

Such situation often appears when the scale length of physical phenomena is larger than that of local update procedures. The case is seen near to a critical point. In fact, the correlation length between components grows extremely close to the critical point, while local update procedures only change components within a fixed area at a time.

The autocorrelation time τ diverges at critical point as follows:

$$\tau \propto L^z, \tag{1.26}$$

where L is the linear dimension of the system and z is a constant called dynamical critical exponent. Usually $z \geq 2$ for local update algorithms. As the system becomes

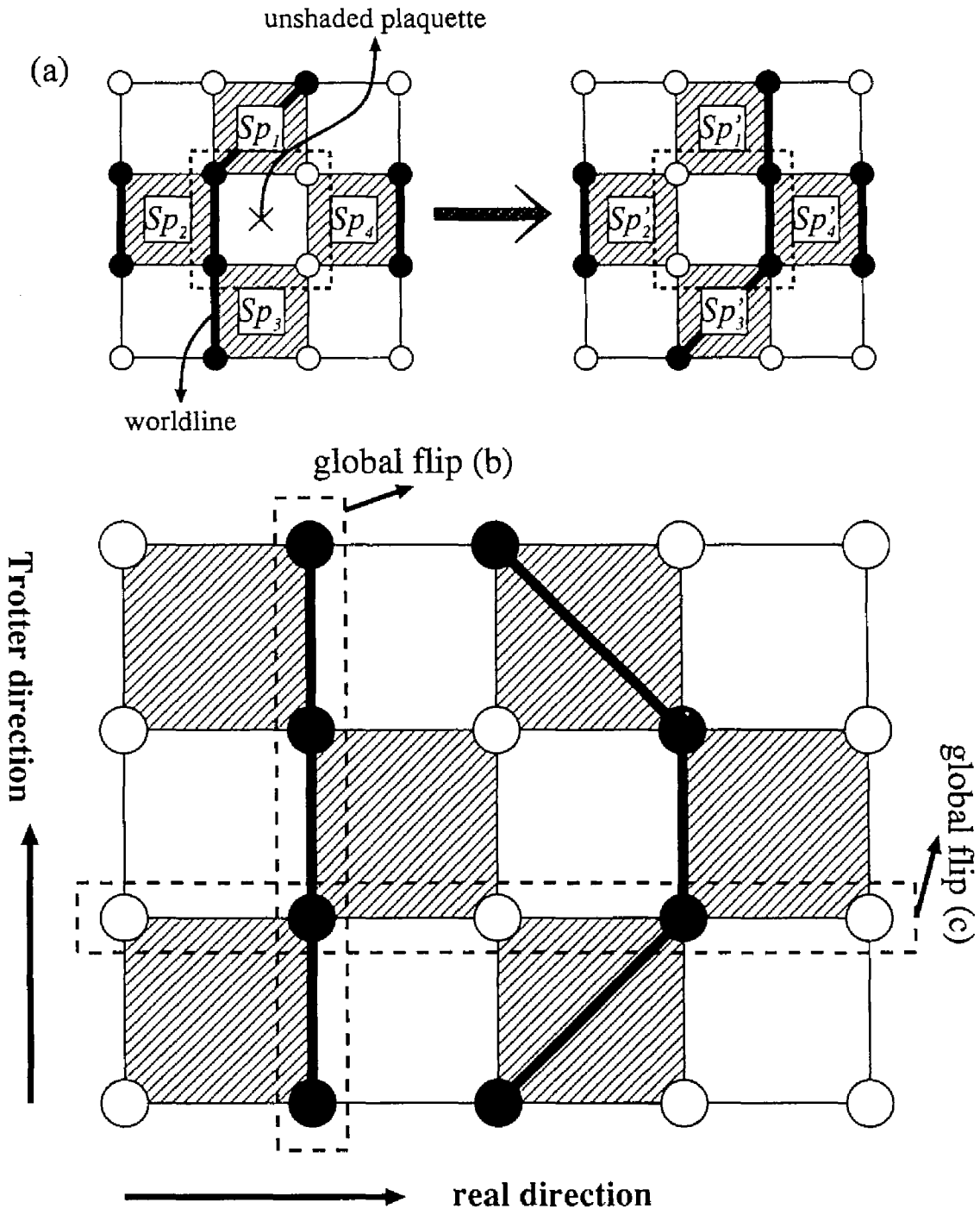

Figure 1.4: A local deformation and two global flips of worldlines. (a) a example for the local deformation. (b) a global flip along Trotter direction. (c) a global flip along real direction.

larger, the autocorrelation time grows rapidly. So it is difficult to keep the statistical error of measured quantities small in Monte Carlo simulations for large systems.

For the worldline algorithm, we see an another reason for the increase of the autocorrelation time. It is related to the systematic error of ST decomposition as Sec. 1.2. In order to keep the error small, the Trotter number m must be large enough. When m is large, the acceptance rate for flips related to non-diagonal elements of two-spin propagator is very small. Almost all configurations get no change and then the autocorrelation time becomes large. It diverges as follows:

$$\tau \propto \left(\frac{m}{\beta}\right)^{z_T}, \tag{1.27}$$

where z_T is a constant, usually $z_T \sim 2$.

Those matters make quantum Monte Carlo simulations difficult to practice for large systems or low temperatures.

Systematic error due to ST decomposition

The worldline algorithm treats a classical model which approximates an original quantum model by ST decomposition accompanied by systematic errors.

Once we obtain a set of data with a fixed temperature and various Trotter numbers, we must do the Trotter extrapolation to the limit $m \to \infty$. The Trotter number m must be enough to ensure the convergence. This causes the above-mentioned increase of the autocorrelation time.

Ergodicity

Some ways of global flips are introduced in the worldline algorithm to ensure the ergodicity of the magnetization or the winding number. But they do not work as are expected. For example, the global flip for the winding number also has low performance at low temperature. The acceptant rate is almost zero, because it depends on non-diagonal elements of Hamiltonian.

Furthermore, it is difficult to implement them on such lattices as bond disorder and depleted lattice, because they are too artificial.

1.4 Loop algorithm

In this section, we discuss two types of loop algorithms: loop algorithm on discrete imaginary time [14] and that on continuous imaginary time [4]. They overcome almost all difficulties of traditional worldline algorithms.

In Sec. 1.4.1, we review a general definition of cluster algorithms by Kandel–Domany framework [20,25]. In Sec. 1.4.2 and Sec. 1.4.3, we discuss loop algorithms on discrete and continuous imaginary time, respectively.

1.4.1 General definition of cluster algorithm

For the Monte Carlo simulation of a classical model, Swendsen and Wang (SW) [40] have invented a new algorithm which is called cluster algorithm.

For illustration of cluster algorithms, we introduce new variables G_p as

$$w_p(S_p) = \sum_{G_p} w_p(S_p, G_p), \qquad w_p(S_p, G_p) \geq 0, \tag{1.28}$$

where G_p is a graph variable defined on a plaquette. The partition function is

$$Z = \sum_S \prod_p w_p(S_p) = \sum_{S,G} \prod_p w_p(S_p, G_p), \tag{1.29}$$

where summation $\sum_G$ extends over all configurations of graph variables.

When a plaquette has N components, the number of breakups of the plaquette $N_b(N)$ is described as

$$N_b(N) \equiv \sum_k^N g(N,k), \tag{1.30}$$

$$\sum_{i=1}^{k} {}_kP_i \; g(N,i) = k^N \qquad (k = 1, \cdots, N). \tag{1.31}$$

If we change spins with a same manner in any breakup peace, then we can get many kinds of spin configurations from one configuration. The value of the graph variable G_p identifies such a group of spin configurations. The number of states of G_p rapidly increases as $O(\alpha^N)$, but this is not so essential in Monte Carlo simulation, because the number of states used in simulations is small.

According to Fortuin and Kasteleyn [21,22], $w(S_p, G_p)$ is rewritten as

$$w_p(S_p, G_p) = A_p(S_p) v_p(G_p) \Delta(S_p, G_p), \tag{1.32}$$

where $\Delta(S_p, G_p) = 1$ if $S_p \in G_p$, and $= 0$ otherwise.

A Markov process generated by a traditional Monte Carlo algorithm stays in the spin configuration space:

$$S^{(1)} \to S^{(2)} \to S^{(3)} \to \cdots, \tag{1.33}$$

whereas a Markov process of a cluster algorithm alternates between the spin and graph configuration spaces:

$$S^{(1)} \to G^{(1)} \to S^{(2)} \to G^{(2)} \to S^{(3)} \to G^{(3)} \to \cdots. \tag{1.34}$$

The transition probabilities between the spin and graph configurations are defined as follows:

$$P(S \to G) \equiv \frac{\prod_p w_p(S_p, G_p)}{\sum_{G'} \prod_p w_p(S_p, G'_p)} \tag{1.35}$$

$$P(G \to S) \equiv \frac{\prod_p w_p(S_p, G_p)}{\sum_{S'} \prod_p w_p(S'_p, G_p)} \tag{1.36}$$

where $S \equiv \bigcup_p S_p$ and $G \equiv \bigcup_p G_p$ are global spin and graph configurations, respectively. Equation (1.35) denotes that each local transition on a plaquette is determined by

$$P(S_p \to G_p) \equiv \frac{w_p(S_p, G_p)}{\sum_{G'_p} w_p(S_p, G'_p)}. \tag{1.37}$$

It is easy to check that these transition probabilities satisfy the detailed balance conditions. Hence the appearance probability of spin configuration S in a Markov chain is

$$P(S) \equiv \frac{1}{Z} \sum_G \prod_p w_p(S_p, G_p) = \frac{1}{Z} \prod_p w_p(S_p). \tag{1.38}$$

That of graph configuration G is

$$P(G) \equiv \frac{1}{Z} \sum_S \prod_p w_p(S_p, G_p). \tag{1.39}$$

Since global graph configuration G only indicates how spins in the system are divided, a spin configuration can be specified among various ones according to eq. (1.36). There are global differences among these spin configurations and such a non-local change in Monte Carlo process is taken out by each local stochastic decision on each plaquette as eq. (1.37). The set of spins to be changed with a same manner is called cluster, and the algorithm updating clusters on system at a same time by eq. (1.36) is called cluster algorithm.

The implementation way of the cluster algorithm on a computer is fairly different from that of the traditional algorithm. In cluster algorithm we need to identify clusters. It corresponds to union-find problem in computer science [1]. Fortunately, its elapse time is almost of linear order of system size with using list data structures and path-compressions.

The cluster algorithm has important advantages in comparison with traditional local update algorithms.

Autocorrelation

The scale of clusters in an efficient cluster algorithm is same as that of physical phenomena: the correlation function of two sites in the model is identical with a function of the probability that those two sites belong to a same cluster. Thus the cluster algorithm greatly reduces the autocorrelation between successive Monte Carlo configurations in many cases. In fact, the dynamical exponent z is very small compared with that of traditional local update algorithms and for quantum models, the autocorrelation time is independent of the Trotter number. So loop algorithms allow us to do quantum Monte Carlo simulations for large systems and low temperatures.

Ergodicity

In order to ensure the ergodicity for quantum models, the worldline algorithm has artificial global updates. The cluster algorithm only takes natural global flips, without any more global flips.

Improved estimator

In general, the cluster algorithm may have improved estimators for various quantities. The details are described in Sec. 1.5.

1.4.2 Loop algorithm on discrete imaginary time

A Monte Carlo simulation for a quantum spin model is replaced by a classical model as eq. (1.8) to be solved as mentioned in Sec. 1.4.1. In this case, it is called loop algorithm on discrete imaginary time, because the shape of clusters is loop-like for the some conservation rules (1.23) and the classical model approximates the quantum model on discrete imaginary time.

In the following, we are going to show an example for the one-dimensional $S = 1/2$ quantum XXZ model.

One-dimensional $S = 1/2$ quantum XXZ model

It is easy to see from eq. (1.28) and eq. (1.32) that $\Delta(S_p, G_p)$ satisfies

$$A(S_p) \sum_{G_p} v(G_p) \Delta(S_p, G_p) = w(S_p). \tag{1.40}$$

It gives that $v(G_p)$ takes zero if $w(S_p)$ is zero and $\Delta(S_p, G_p)$ is one. Since eq. (1.37) makes the transition probability from any S_p to such G_p to be zero, such G_p is not so essential to be considered. The number of essential breakups for the $S = 1/2$ quantum XXZ model are only four in Fig. 1.5.

The breakup $G_p = 4$ in Fig. 1.5 is called freezing breakup, because it freezes four spins. The other breakup divides a plaquette into two pieces. The freezing breakup makes larger clusters than the other. From experiences, an efficient cluster algorithm is to keep the scale of clusters small. Thus the transition probability to the freezing breakup had better be small.

We represent $\Delta(S_p, G_p)$ by matrixes as eq. (1.21):

$$\Delta(\cdot, 1) = \begin{pmatrix} 1 & 0 & 0 & 0 \\ 0 & 1 & 0 & 0 \\ 0 & 0 & 1 & 0 \\ 0 & 0 & 0 & 1 \end{pmatrix}, \Delta(\cdot, 2) = \begin{pmatrix} 0 & 0 & 0 & 0 \\ 0 & 1 & 1 & 0 \\ 0 & 1 & 1 & 0 \\ 0 & 0 & 0 & 0 \end{pmatrix},$$

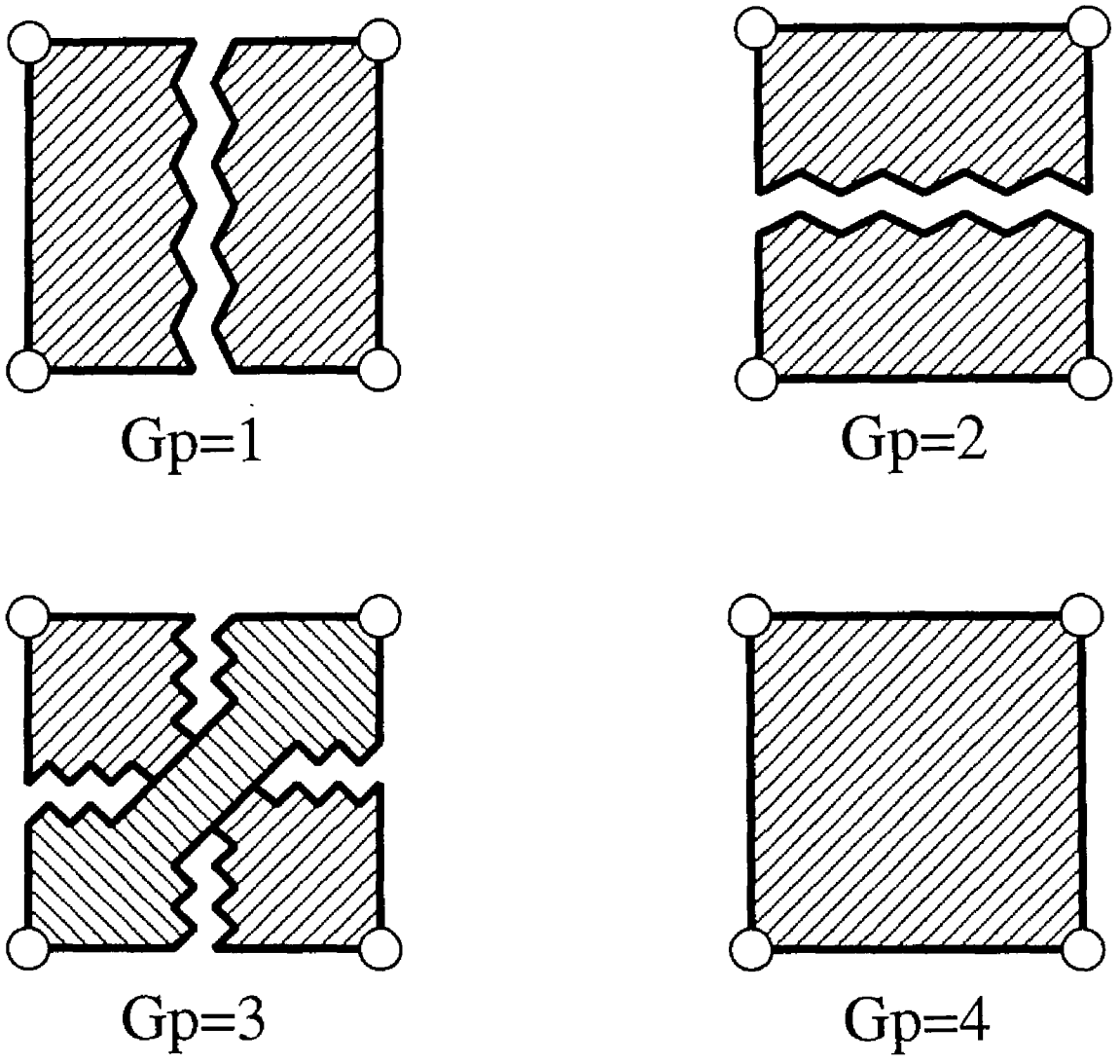

Figure 1.5: Breakups for $S = 1/2$ quantum XXZ model.

$$\Delta(\cdot,3) = \begin{pmatrix} 1 & 0 & 0 & 0 \\ 0 & 0 & 1 & 0 \\ 0 & 1 & 0 & 0 \\ 0 & 0 & 0 & 1 \end{pmatrix}, \Delta(\cdot,4) = \begin{pmatrix} 1 & 0 & 0 & 0 \\ 0 & 0 & 0 & 0 \\ 0 & 0 & 0 & 0 \\ 0 & 0 & 0 & 1 \end{pmatrix}. \tag{1.41}$$

From eq. (1.40), $A(S_p)$ is found as

$$A \equiv \begin{pmatrix} e^{\frac{\beta}{2m}B} & 0 & 0 & 0 \\ 0 & 1 & 1 & 0 \\ 0 & 1 & 1 & 0 \\ 0 & 0 & 0 & e^{-\frac{\beta}{2m}B} \end{pmatrix}, \tag{1.42}$$

and $v(G_p)$ is also found as in Table 1.1.

Table 1.1: $v(G_p)$ for $S = 1/2$ quantum XXZ model on discrete imaginary time.

G_p	$v(G_p)$
1	$\frac{1}{2}\left(e^{\frac{\beta}{4m}J_z} + e^{-\frac{\beta}{4m}J_z}e^{-\frac{\beta}{2m}J_x} - v(4)\right)$
2	$\frac{1}{2}\left(e^{-\frac{\beta}{4m}J_z}e^{\frac{\beta}{2m}J_x} - e^{\frac{\beta}{4m}J_z} + v(4)\right)$
3	$\frac{1}{2}\left(e^{\frac{\beta}{4m}J_z} - e^{-\frac{\beta}{4m}J_z}e^{-\frac{\beta}{2m}J_x} - v(4)\right)$
4	$\max\left(0, e^{\frac{\beta}{4m}J_z} - e^{-\frac{\beta}{4m}J_z}e^{\frac{\beta}{2m}J_x}\right)$

This algorithm divides spins into a number of loops as Fig. 1.6, which are independent each other. Table 1.1 tells that the freezing breakup frequently appears when $J_x < J_z$. Hence the average size of a loop may become large, as expected for this model.

1.4.3 Loop algorithm on continuous imaginary time

In a continuous limit ($\beta/m \to 0$), the worldline is continuous almost everywhere along the Trotter direction and it may sometimes jump to a neighbor site. Since the jump is instantaneous, the worldline configuration is described by specifying the imaginary times at which worldlines jump. In the following, we show the loop algorithm on plaquettes whose imaginary time interval is infinitesimal.

Partial Hamiltonian $\hat{H}_i$ can be directly represented by the graph variable G_p as

$$\langle C_t | \hat{H}_i | C_{t+1} \rangle \equiv -\sum_{G_p} a_p(G_p)\Delta(S_p, G_p) - B_p(S_p), \tag{1.43}$$

where $\Delta(S_p, G_p)$ is same as in the previous section.

If $\epsilon \equiv \beta/m \ll 1$, $w_p(S_p)$ takes the form

$$w_p(S_p) \equiv \langle C_t | e^{-\epsilon \hat{H}_i} | C_{t+1} \rangle \approx e^{-\epsilon B_p(S_p)}[I_p(S_p) + \epsilon \sum_{G_p} a_p(G_p)\Delta(S_p, G_p)], \tag{1.44}$$

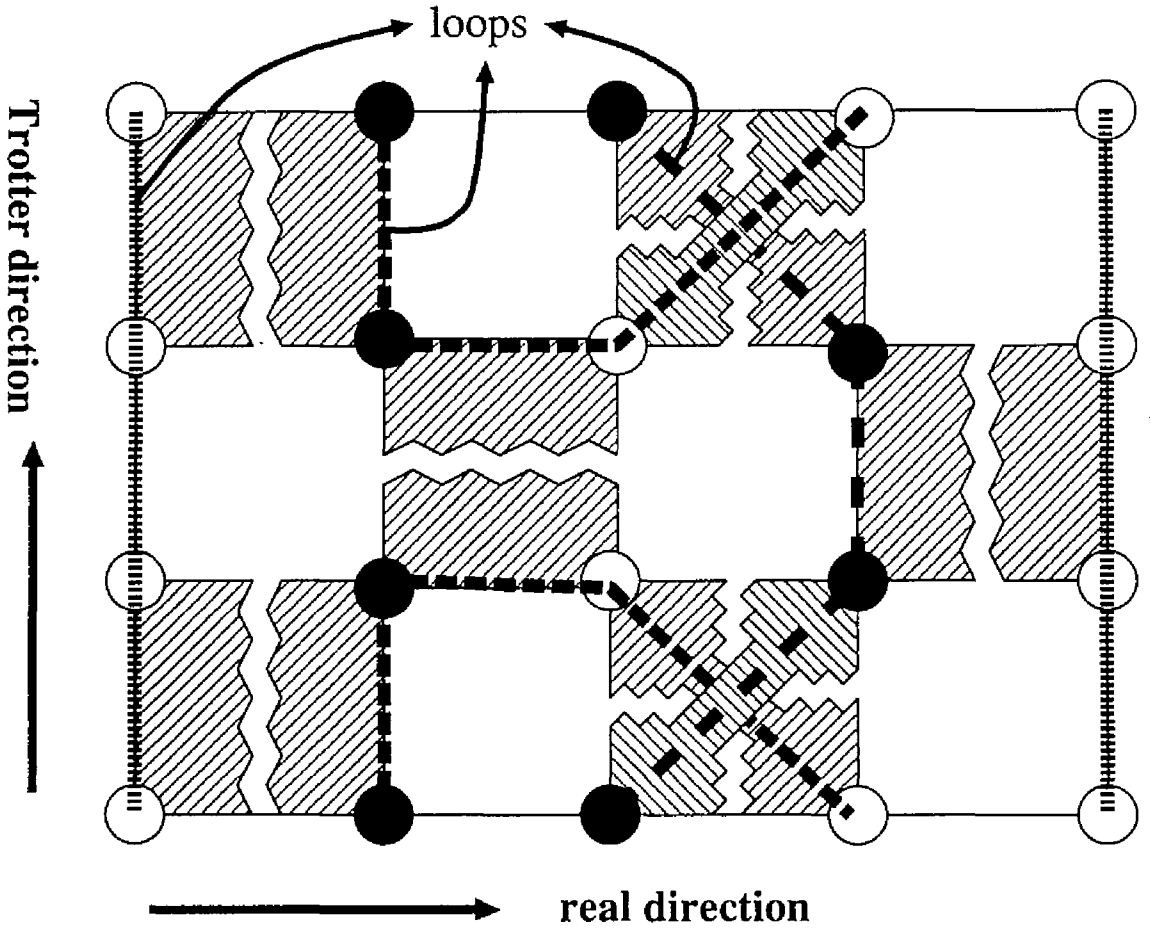

Figure 1.6: Loops on the checker-board square lattice.

where $I_p(S_p)$ is the identity operator on a plaquette. For simplicity, we take $\Delta(S_p, 1) \equiv I_p(S_p)$ in the following.

Taking the limit of an infinitesimal imaginary time spacing ($\epsilon \to 0$), the transition probability (eq. (1.37)) on a plaquette is reduced to the followings:

(i) If the present state S_p is compatible to the graph $G_p = 1$, i.e., if there is no exchange of spins in the time interval $(t, t+\epsilon)$,

$$\begin{aligned} &P(S_p \to G_p) = \epsilon a_p(G_p)\Delta(S_p, G_p) \quad (G_p \neq 1), \\ &P(S_p \to 1) = 1 - \sum_{G'_p \neq 1} P(S_p \to G'_p). \end{aligned} \tag{1.45}$$

(ii) If the present state S_p is incompatible to the graph $G_p = 1$, i.e., if the state at t is different from that at $t+\epsilon$,

$$\begin{aligned} &P(S_p \to G_p) = \frac{a_p(G_p)\Delta(S_p, G_p)}{\sum_{G'_p \neq 1} a_p(G'_p)\Delta(S_p, G'_p)} \quad (G_p \neq 1), \\ &P(S_p \to 1) = 0 \end{aligned} \tag{1.46}$$

We apply eq. (1.45) to plaquettes (with infinitesimal "heights") at which worldlines continue along the Trotter direction. The probability of choosing a graph $G_p \neq 1$ in the imaginary time interval ϵ is $\epsilon a_p(G_p)\Delta(S_p, G_p)$. This means that in the continuous limit we distribute graphs G_p over such an interval uniformly, i.e., with a Poisson process, with the probability density $a_p(G_p)\Delta(S_p, G_p)$. On the other hand, eq. (1.46) gives the probability (not probability density) with which a graph is assigned to each point of time where the local state is changed or two neighboring worldlines are exchanged.

Consequently, for general models, the loop algorithm with continuous imaginary time can be summarized as follows. For each pair of nearest neighbor worldlines,

(i) distribute graphs $G_p(\neq 1)$ with a Poisson process with eq. (1.45) over every imaginary time interval in which worldlines are not interrupted,

(ii) choose a graph G_p with eq. (1.46) at each point of time where states are exchanged between the two sites,

(iii) assign the graph $G_p = 1$ elsewhere,

and then update spin values by flipping clusters (eq. (1.36)).

This algorithm have several important advantages in comparison with that on discrete imaginary time as follows.

Systematic error due to ST decomposition

With a finite Trotter number m, we have systematic errors due to ST decomposition. To reduce them, we must take the Trotter extrapolation, while in the continuous limit it is not necessary. This feature is important to carry out quantum Monte Carlo simulation in low temperature, because the Trotter number m is usually so large to suppress those systematic errors in low temperatures.

Implementation on computer

Memory capacity to keep worldline configurations can be reduced by a technique of specifying a imaginary time at which worldlines jump. Furthermore, its implementation is sometimes steeply simpler than that on discrete imaginary time. We will show a good example of a higher spin case in detail in Chap. 3.

$S = 1/2$ quantum XXZ model

We here illustrate an example of the $S = 1/2$ quantum XXZ model.

From eq. (1.43), $B(S_p)$ is found as

$$B(S_p) \equiv \begin{pmatrix} \frac{B}{2} & 0 & 0 & 0 \\ 0 & 0 & 0 & 0 \\ 0 & 0 & 0 & 0 \\ 0 & 0 & 0 & -\frac{B}{2} \end{pmatrix}, \tag{1.47}$$

and $a(G_p)$ is also found as in Table 1.2. In this case, $a(1)$ is negative. Its value is however not used (see eq. (1.45) and eq. (1.46)).

Table 1.2: $a(G_p)$ for $S = 1/2$ quantum XXZ model on continuous imaginary time.

G_p	$a(G_p)$
1	$-\frac{1}{4}J_x - \frac{1}{2}a(4)$
2	$\frac{1}{4}(J_x - J_z) + \frac{1}{2}a(4)$
3	$\frac{1}{4}(J_x + J_z) - \frac{1}{2}a(4)$
4	$\max\left(0, \frac{1}{2}(J_z - J_x)\right)$

1.5 Improved estimator

We will introduce new estimators of various quantities, which deserve the so-called improved estimators. In fact, they can reduce the statistical errors of measured quantities. In the present section, we first define a general improved estimator in cluster algorithms and discuss its performance.

1.5.1 Definition of improved estimator

If we denote a normal estimator of a quantity by $f(S)$, which is defined as a function of spin variables S, then the corresponding new estimator is defined as

$$f(G) \equiv \frac{\sum_S f(S)W(S,G)}{\sum_S W(S,G)}, \tag{1.48}$$

where $W(S,G) \equiv \prod_p w_p(S_p, G_p)$.

From eq. (1.38) and eq. (1.39), the average of the estimator $f(G)$ is equal to that of the normal estimator $f(S)$:

$$\langle f(G) \rangle = \langle f(S) \rangle, \tag{1.49}$$

where

$$\langle X \rangle \equiv \sum_{S,G} X\ W(S,G) / \sum_{S,G} W(S,G). \tag{1.50}$$

In (1.48) we calculate the average over the $O(\alpha^{N_c})$ states in a time, where N_c is the number of clusters in a graph configuration G. This is a reason that the estimator (1.48) is improved from normal one. Fortunately, we can easily calculate it as follows.

For example, various quantities as susceptibility, static structure factor and helicity modulus are defined by the following form,

$$A^2(S) \equiv \left(\sum_i \alpha_i S_i \right)^2, \tag{1.51}$$

where α_i is a constant and S_i is the spin variable at site i. The improved estimator is defined as

$$A^2(G) \equiv \sum_c A_c^2, \tag{1.52}$$

with

$$A_c \equiv \sum_{i \in c} \alpha_i S_i, \tag{1.53}$$

where c identifies each cluster in the graph configuration G and summation $\sum_c$ extends over all clusters in G. Though the estimator is given as the average over $O(\alpha^{N_c})$ states, they are easily calculated.

1.5.2 Variance of improved estimator

It must be noted that the improved estimator has smaller variance than that of the normal estimator. In the following, we explicitly evaluate the variance of general improved estimators.

The normal estimator $A^2(S)$ is decomposed into two parts:

$$A^2(S) = \sum_c A_c^2 + \sum_{c \neq c'} A_c A_{c'} = A^2(G) + A_{rem}^2, \tag{1.54}$$

where A^2_{rem} is defined as $\sum_{c \neq c'} A_c A_{c'}$. For simplicity, symbol $\mathcal{O}$, $\mathcal{O}_{impr}$ and $\mathcal{O}_{rem}$ denote the normal estimator, improved estimator and A^2_{rem}, respectively.

Since clusters are flipped independently in SW algorithm, the expectation values of all the cross terms in $\mathcal{O}_{rem}$ are vanishing. Therefore,

$$\langle \mathcal{O}_{rem} \rangle = 0. \tag{1.55}$$

For the same reason, we can derive another useful equation,

$$\langle \mathcal{O}_{impr} \cdot \mathcal{O}_{rem} \rangle = 0. \tag{1.56}$$

Equation (1.55) leads to

$$\langle \mathcal{O} \rangle = \langle \mathcal{O}_{impr} \rangle. \tag{1.57}$$

This implies that the $\mathcal{O}_{impr}$ is another estimator. The new estimator $\mathcal{O}_{impr}$ depends only on the graph variables.

One graph configuration represents 2^{N_c} spin configurations. Therefore, a sampling of $\mathcal{O}_{impr}$ corresponds to taking an averaged value over many samplings of $\mathcal{O}$. From eq. (1.56), the variance of $\mathcal{O}$ is related to those of $\mathcal{O}_{impr}$ and $\mathcal{O}_{rem}$ as

$$\begin{aligned} \mathrm{Var}(\mathcal{O}) &= \langle (\mathcal{O}_{impr} + \mathcal{O}_{rem})^2 \rangle - \langle \mathcal{O}_{impr} + \mathcal{O}_{rem} \rangle^2 && (1.58) \\ &= \mathrm{Var}(\mathcal{O}_{impr}) + \mathrm{Var}(\mathcal{O}_{rem}) && (1.59) \\ &\geq \mathrm{Var}(\mathcal{O}_{impr}). && (1.60) \end{aligned}$$

The performance of an estimator is related with the variance (1.25), and hence the estimator $\mathcal{O}_{impr}$ is surely improved one.

We here have introduced the improved estimator for quantum models based on the discrete time representation. We can use the same definition in the continuous time representation as well.

2. Kosterlitz-Thouless transition of $S = 1/2$ quantum XY model in two dimensions

2.1 Introduction

The XY model in two dimensions has been discussed in various contexts such as magnets with easy-plane anisotropy, superconductivity in a thin layer, granular superconducting materials, and insulator-superfluid transition in He^4 systems. Naturally, a number of works were devoted to clarifying the nature of the phase transition and the low-temperature phase of this model. Among them notable was a large scale Monte Carlo simulation by Ding and Makivić [12,32]. Based on computation of the linear in-plane susceptibility and the correlation length at various temperatures, they concluded that a phase transition takes place at $T_{\mathrm{KT}} = 0.350(4)$ [12,32] or 0.353(3) [10], and that this transition is of Kosterlitz–Thouless (KT) [30] type. However, it is technically difficult to distinguish an exponential divergence from an algebraic one. Because of this difficulty, the validity of their conclusion on the nature of the phase transition was questioned [11,41]. For the same reason, in spite of their very extensive Monte Carlo calculation, Gupta and Baillie [16,17] did not draw a definitive conclusion although their numerical results seemed to suggest that the phase transition of the classical XY model is exactly what the KT theory predicts.

It should be noted that the above-mentioned technical difficulty is partially due to the absence of finite-size-scaling type analysis which is a common and powerful tool in most numerical studies. However, Solýom and Ziman [38] pointed out that the straightforward application of the ordinary finite-size-scaling analysis leads to a wrong result not only when the power-law temperature dependence of the correlation length, which is wrong, is assumed but also when the correct exponential divergence is assumed. They studied the size dependence of the first excitation gap in the $S = 1/2$ anisotropic XXZ model in one dimension, which is exactly solvable and known to have a transition of the KT type at the antiferromagnetic isotropic point. They found that the exact estimates for the finite systems do not fit into the standard form of the finite-size-scaling at the critical point.

Therefore, to obtain a definitive answer to the question concerning the nature of the phase transition, we need to have a correct form for the system size dependence of quantities of interest. In previous studies, to our knowledge, a systematic study

of such system size dependence has been missing for the quantum XY model. There are, however, some reports on classical XY models. Instead of using the ordinary finite-size-scaling form, Weber and Minnhagen [44] used the Kosterlitz renormalization group equation [29] for the data analysis in their study of the classical XY model in two dimensions. They verified the KT type phase transition by comparing the size dependence of the helicity modulus, Υ, at the critical temperature with the renormalization group flow along the critical line that converges to the KT fixed point with a logarithmically slow convergence. They observed not only that the computed helicity modulus exhibits the logarithmic dependence on the length scale but also that even the pre-factor of this logarithmic term agreed with the predicted one. Following the same idea, Olsson [36] performed a more detailed analysis of the classical model with an extensive Monte Carlo simulation. He observed that the system-size dependence of the helicity modulus agreed with the form derived from the Kosterlitz renormalization group equation below and above the critical temperature as well as right at the critical temperature.

The helicity modulus is known to exhibit the universal jump at the critical temperature [35]. This quantity corresponds to the super-fluid density when the model is regarded as a Boson system with hard-cores. In the worldline quantum Monte Carlo method, the helicity modulus is represented as the fluctuation in the total winding number of worldlines by the following equation [37],

$$\Upsilon = (T/2)\langle \mathbf{W}^2 \rangle, \tag{2.1}$$

where $\mathbf{W} \equiv (W_x, W_y)$ with W_x (W_y) being the total winding number in the x (y) direction. It is difficult to measure this quantity by means of a conventional worldline quantum Monte Carlo method because a conventional algorithm is not ergodic in that the winding number is not allowed to vary. In principle, it is possible to make it ergodic by introducing additional global movements of worldlines. In practice, however, such additional and in most cases "ad-hoc" global movements are seldom accepted and the resulting estimates of the helicity modulus have large statistical errors. Therefore, Makivić [31] divided the whole system into a number of sub-systems and measured the winding number for each sub-system which may vary. It is not totally clear if this alternative way of measurement gives the same answer as the conventional one does. Another difficulty of the conventional Monte Carlo method is its long autocorrelation time near and below the critical temperature. These difficulties limited the accuracy and the precision of the Makivić's estimates of the helicity modulus and narrowed the accessible temperature range of simulation.

In the present study, we report some results of the quantum Monte Carlo simulation of the $S = 1/2$ XY model using the loop algorithm [14,23] with both discrete and continuous imaginary time representations [4]. The use of the loop algorithm eliminates both of the above-mentioned difficulties. There the number of particles as well as the winding number can vary. At the same time, there are a number of reports [23] on the drastic improvement in the autocorrelation time of the simulation by loop algorithms. We aim at a detailed and precise comparison between the

quantum XY model and the theory by Kosterlitz [29] through an accurate estimation of the thermal fluctuation in the winding number near and below the critical temperature. We show that such an estimation allows us to examine a new scaling form different from the ordinary finite-size-scaling. In this scaling form, the distance from the critical point, i.e., $K - K_{\rm KT}$ appears in the form of $(K - K_{\rm KT})(\log(L/L_0))^2$, in contrast to $(K - K_{\rm KT})L^{y_T}$ in the ordinary finite-size-scaling. At the same time, the quantity $x \equiv \langle(\pi/2)\mathbf{W}^2\rangle - 2$ scales as $x \log(L/L_0)$ rather than x/L^{ω} with some exponent ω. This "scaling" form is consistent with Olsson's fitting functions.

In Sec. 2.2, we describe loop algorithms on discrete and continuous imaginary time. In Sec. 2.3, the definition of helicity modulus, its improved estimator and details of simulations are described. In Sec. 2.4, estimates of the helicity modulus are presented and we summarize the results in Sec. 2.5.

2.2 Loop algorithm for $S = 1/2$ quantum XY model

The $S = 1/2$ quantum XY model is defined by the following Hamiltonian.

$$\hat{H} = \sum_{\langle ij \rangle} \hat{H}_{ij} = -J \sum_{\langle ij \rangle} (\hat{S}_i^x \hat{S}_j^x + \hat{S}_i^y \hat{S}_j^y), \tag{2.2}$$

where $\langle ij \rangle$ runs over all nearest-neighbor pairs on a square lattice. As for the spin operators, we use the convention in which $(\hat{S}_i^{\mu})^2 = 1/4$ $(\mu = x, y, z)$. We will take J as the unit of the energy scale in what follows.

Our Hamiltonian can be considered as a sum of four sub-Hamiltonians: $\hat{H} = \hat{H}_A + \hat{H}_B + \hat{H}_C + \hat{H}_D$. Each sub-Hamiltonian is a sum of operators commutable with each other, i.e.,

$$\hat{H}_X = \sum_{\langle ij \rangle \in X} \hat{H}_{ij} \quad (X = A, B, C, D) \tag{2.3}$$

where

$$A \equiv \{\langle ij \rangle | i \in \text{odd column}, j = i + e_x\}, \tag{2.4}$$
$$B \equiv \{\langle ij \rangle | i \in \text{odd row}, j = i + e_y\}, \tag{2.5}$$
$$C \equiv \{\langle ij \rangle | i \in \text{even column}, j = i + e_x\}, \tag{2.6}$$
$$D \equiv \{\langle ij \rangle | i \in \text{even row}, j = i + e_y\}, \tag{2.7}$$

and e_x (or e_y) is a unit lattice vector in the x (or y) direction.

Using the ST decomposition, we transform the partition function into the following form,

$$Z \approx \sum_S \prod_p w(S_p). \tag{2.8}$$

Here, p stands for a plaquette in the $(d+1)$-dimensional space-time with two edges perpendicular and the other two parallel to the imaginary time axis. The space-time

location of its left-bottom corner is given by (i, t) with

$$t \equiv \begin{cases} (4n)\Delta\tau & \text{if } i \in A \\ (4n+1)\Delta\tau & \text{if } i \in B \\ (4n+2)\Delta\tau & \text{if } i \in C \\ (4n+3)\Delta\tau & \text{if } i \in D \end{cases}, \tag{2.9}$$

where the imaginary time spacing, $\Delta\tau \equiv \beta/m$, is the unit of the discretization of the imaginary time. The number of steps m is called the Trotter number. The symbol S_p in eq. (2.8) is the local spin configuration on a plaquette p and $w(S_p)$ is the two-spin propagator defined below. The symbol S in eq. (2.8) stands for the spin configuration of the whole space-time or the union of all S_p's, i.e., $S \equiv \bigcup_p S_p$. We denote the four states of spin pairs by $1 = \uparrow\uparrow$, $2 = \uparrow\downarrow$, $3 = \downarrow\uparrow$ and $4 = \downarrow\downarrow$. Then, the two-spin propagator can be written explicitly as

$$\begin{aligned} w(S_p) &\equiv \left\langle S_p^{(\text{final})} \left| \exp\left(-(\Delta\tau)\hat{H}_{ij}\right) \right| S_p^{(\text{initial})} \right\rangle \\ &= \begin{pmatrix} 1 & 0 & 0 & 0 \\ 0 & \cosh(\frac{\Delta\tau J}{2}) & \sinh(\frac{\Delta\tau J}{2}) & 0 \\ 0 & \sinh(\frac{\Delta\tau J}{2}) & \cosh(\frac{\Delta\tau J}{2}) & 0 \\ 0 & 0 & 0 & 1 \end{pmatrix}. \end{aligned} \tag{2.10}$$

The symbol $S_p^{(\text{initial})}$ and $S_p^{(\text{final})}$ stand for the local state of two corners at the bottom and top edges of the plaquette p, respectively. The local state of the whole plaquette, S_p, can be regarded as the combination of the two. In the 4×4 matrix representation of eq. (2.10), the column index corresponds to four possible initial state, $S_p^{(\text{initial})}$, and the row index $S_p^{(\text{final})}$.

2.2.1 On discrete imaginary time

With using the notation in Sec. 1.4.2, the loop algorithm on discrete imaginary time is specified by $A(S_p) = 1$ and $v(G_p)$ in Table 2.1.

Table 2.1: $v(G_p)$ for $S = 1/2$ quantum XY model on discrete imaginary time.

G_p	$v(G_p)$
1	$\frac{1}{2}(e^{-\frac{\Delta\tau}{2}J} + 1)$
2	$\frac{1}{2}(e^{\frac{\Delta\tau}{2}J} - 1)$
3	$\frac{1}{2}(1 - e^{-\frac{\Delta\tau}{2}J})$

We see from eq. (1.36) that $P(G \to S)$ is vanishing if S_p is not compatible to G_p for any p, while it takes a value independent of S as long as all S_p's are compatible to G_p's. This means that sites belonging to the same loop should be

flipped simultaneously with a probability 1/2, and two distinct loops should be flipped independently. Since flipping a loop is a global update, one may imagine that the cluster algorithm reduces the autocorrelation time due to slow relaxation modes associated with large structures. This is indeed the case as reported in a number of articles [23].

In this case, the Markov process is also ergotic, that is, the winding number can vary in our Monte Carlo simulation.

2.2.2 On continuous imaginary time

The loop algorithm on continuous imaginary time is specified by $B(S_p) = 0$ and $a(G_p)$ in Table 2.2.

Table 2.2: $a(G_p)$ for $S = 1/2$ quantum XY model on continuous imaginary time.

G_p	$a(G_p)$
1	$-\frac{1}{4}J$
2	$\frac{1}{4}J$
3	$\frac{1}{4}J$

The graph assignment in this algorithm is simple as follows:

(i) for each uninterrupted time interval during which spins on these worldlines are antiparallel, generate "horizontal reconnections" (graph $G_p = 2$ in Fig. 1.5) of worldlines with probability density $J/4$, and for parallel spins, generate "diagonal reconnections" (graph $G_p = 3$) of worldlines with probability density $J/4$,

(ii) at each point of time where worldlines exchange, assign a horizontal or diagonal reconnection with equal probability (1/2),

(iii) assign the graph $G_p = 1$ elsewhere.

2.3 Quantum Monte Carlo simulation

2.3.1 Helicity modulus

In the present study, we focus on the helicity modulus because it may be directly related to the solution of the Kosterlitz renormalization group equation and therefore may exhibit some behavior characteristic of the KT transition. We have measured the helicity modulus by computing the fluctuation in the total winding number of worldlines with eq. (2.1). The total winding number W_x (or W_y) is defined as the sum of winding numbers of individual worldlines. The winding number of an

individual worldline is the number of times the worldline wraps around the system in the x or y direction before coming back to its starting point. The total winding number of worldlines for up spins is exactly the same in magnitude as that for down spins and has the opposite sign. We here count only the winding numbers for up spins. Alternatively, W_x can be defined as

$$W_x = \frac{1}{L_x} \sum_p \alpha_x(S_p),$$
$$\frac{1}{L_x} \alpha_x(S_p) \equiv \sum_{i \in p} \alpha_i^x S_i^z, \tag{2.11}$$

where L_x is the lattice size in the x direction. The symbol $\alpha_x(S_p)$ stands for the function which takes on the value 1 (or -1) if an up-spin worldline passes through the plaquette p in the positive (or negative) x direction and takes on the value 0, otherwise. Equivalently, α_i^x is a constant which only depends on site i and takes on the value $\pm 1/4$ or zero. To be more specific, $\alpha_i^x = 1/4$ when the site i locates at the lower-left or upper-right corner of a shaded plaquette and $\alpha_i^x = -1/4$ otherwise. (Which is 'left' is an irrelevant question here as it is a matter of the overall sign of the winding number and we are interested only in its squared value.) The other winding number W_y can be also calculated in the same manner.

2.3.2 Improved estimator of helicity modulus

From eq. (2.11), the improved estimator for W_x^2 is

$$(W_x^2)_{impr}(G) \equiv \sum_c (W_{x,c})^2, \tag{2.12}$$

where c denotes a loop and $W_{x,c}$ is defined as

$$W_{x,c} \equiv \frac{1}{L_x} \sum_{i \in c} \alpha_i^x S_i^z. \tag{2.13}$$

The $W_{x,c}$ simply equals to a half of winding numbers of a loop c. The improved estimator for W_y^2 is defined in the same manner.

We compared the error between the normal and the improved estimator in long runs at various temperatures. We found that the improved estimator reduces errors in about twenty per cent and the total performance of the new estimator is 1.5 times better than that of the conventional one in terms of the computational time required.

2.3.3 Simulations

In what follows, we present numerical results both from our older set of simulations performed with a discrete time version of the code and from our newer set with

a continuous time version. We have taken various temperatures between 0.22 and 0.60 and used lattices with $L = 8, 12, 16, 24, 32, 48, 64, 96$ and 128 in our simulation. For simulations with the discrete time version, we have used $m = 8, 16$ and 32 for the Trotter number. When the systematic error of Trotter discretization exceeds the statistical error, we have reduced the systematic error by the extrapolation to $m = \infty$ using three different Trotter numbers. For $L = 12, 24, 48, 96$ and 128 at all temperatures and for all L's near the critical temperature, we have used the continuous time version.

The length of a typical run on $L = 128$ at each temperature is more than 10^6 Monte Carlo sweeps (MCS). The most time-consuming part in the entire code is the cluster identification. It is a task of assigning each spin a number that specifies which cluster the spin belongs to. In doing this, we only use the information of the local connectivity. To make a good use of vector processors for this kind of task, we need to use a vectorizable algorithm. For the discrete version of the code, we adopted an efficient vectorized code following Mino's idea [33]. This idea is based on the "divide-and-conquer" strategy. In this strategy, we firstly divide the lattice into many small sub-lattices and identifies clusters in each sub-lattice neglecting the connectivity outside of the cluster. This process can be easily vectorized or parallelized because cluster identifications of different sub-lattices are independent of each other. We then combine two adjacent original sub-lattices to form a larger sub-lattice and identify clusters in this sub-lattice. In doing this, we can use the information of the clusters in the smaller sub-lattices which have already been obtained in the previous step. We repeat this procedure until all the sub-lattices are combined into a single lattice, i.e., the original whole lattice. Using this algorithm, we achieved the efficiency of 1.5 million site updates per second per one vector processor of Fujitsu VPP500. For the loop algorithm on continuous imaginary time, we used a parallel computer and took trivial parallel approach. Our code does about $29000/(L^2\beta)$ sweeps per second on a node of Hitachi SR2201.

In our simulations, each run is divided into several bins. The length of a bin is taken large enough so that bin averages may be statistically independent from each other at least approximately. In order to check this condition, we have measured autocorrelation times of the improved estimator of the squared winding number at low temperatures $T < 0.35J$ by the standard binning analysis for a run of 10^5 MCS with $L = 64$. They turned out to be smaller than 2 MCS in all cases. We have not observed any difficulty due to low temperature except that, trivially, the computational time per one Monte Carlo step increases proportional to the inverse temperature. The statistical independence among bins is assured, because the smallest bin length used is 1000 MCS. An error bar shown in the figures in the present study represents one standard deviation. Results of the squared winding number $\langle \mathbf{W}^2 \rangle$ are summarized in Table 2.3.

Table 2.3: Squared winding number $\langle \mathbf{W}^2 \rangle$.

T/J	$L = 8$	$L = 16$	$L = 32$	$L = 64$
0.220		2.429(3)	2.433(6)	2.41(2)
0.240		2.214(3)	2.225(5)	2.22(2)
0.260		2.040(3)	2.046(5)	2.05(2)
0.280		1.876(2)	1.865(4)	1.86(2)
0.300		1.728(2)	1.722(4)	1.73(2)
0.320		1.592(2)		1.57(1)
0.325	1.582(1)	1.557(2)	1.540(3)	1.538(5)
0.330	1.552(1)	1.524(2)	1.508(3)	1.493(3)
0.332	1.542(1)	1.510(2)	1.492(3)	1.478(3)
0.334	1.528(1)	1.492(2)	1.478(3)	1.471(3)
0.335	1.521(1)	1.489(2)	1.471(2)	1.454(3)
0.336	1.518(1)	1.483(1)	1.463(2)	1.450(2)
0.337	1.508(1)	1.475(1)	1.455(2)	1.446(2)
0.338	1.505(1)	1.466(1)	1.444(2)	1.433(2)
0.339	1.500(1)	1.4617(9)	1.442(1)	1.425(1)
0.340	1.491(1)	1.4556(9)	1.434(1)	1.418(1)
0.341	1.486(1)	1.4480(9)	1.426(1)	1.407(1)
0.342	1.480(1)	1.4417(9)	1.419(1)	1.400(1)
0.343	1.4727(9)	1.4374(9)	1.409(1)	1.392(1)
0.344	1.4682(9)	1.4292(8)	1.403(1)	1.385(1)
0.345	1.4633(9)	1.4214(9)	1.396(1)	1.377(1)
0.346	1.4571(9)	1.4149(9)	1.388(1)	1.366(1)
0.347	1.451(1)	1.408(1)	1.384(2)	1.359(2)
0.348	1.445(1)	1.401(1)	1.370(2)	1.348(2)
0.349	1.439(1)	1.396(1)	1.365(2)	1.342(2)
0.350	1.433(1)	1.391(1)	1.356(2)	1.334(2)
0.351	1.426(1)	1.379(2)	1.348(2)	1.319(2)
0.352	1.423(1)	1.376(1)	1.338(2)	1.309(2)

Table 2.3: Squared winding number $\langle \mathbf{W}^2 \rangle$ (continued).

T/J	$L = 8$	$L = 16$	$L = 32$	$L = 64$
0.353	1.417(1)	1.369(1)	1.337(2)	1.308(2)
0.354	1.412(1)	1.360(1)	1.327(2)	1.298(3)
0.355	1.403(1)	1.354(2)	1.322(2)	1.286(3)
0.356	1.395(2)	1.349(2)	1.311(2)	1.280(5)
0.357	1.393(2)	1.336(2)	1.302(2)	1.270(5)
0.358	1.386(2)	1.336(2)	1.298(2)	1.262(5)
0.359	1.380(2)	1.330(2)	1.284(2)	1.255(5)
0.360	1.373(1)	1.322(2)	1.279(2)	1.247(4)
0.362	1.368(2)	1.305(3)	1.260(2)	1.21(1)
0.364	1.356(2)	1.296(2)	1.246(2)	1.20(1)
0.366	1.340(2)	1.280(2)	1.227(2)	1.18(2)
0.368	1.328(2)	1.262(2)	1.207(2)	1.14(1)
0.370	1.318(2)	1.249(2)		
0.375	1.290(2)	1.214(2)		
0.380	1.259(1)	1.180(2)		
0.390	1.203(1)	1.105(2)		
0.400	1.146(1)	1.024(2)	0.872(2)	0.65(1)
0.420	1.033(1)	0.856(2)	0.598(2)	0.242(6)
0.440	0.917(1)	0.676(2)	0.328(2)	0.050(3)
0.460	0.804(1)	0.492(2)	0.142(1)	0.007(1)
0.480	0.686(1)	0.338(2)	0.0518(7)	0.0008(3)
0.500	0.579(1)	0.214(1)	0.0171(4)	
0.520	0.479(1)			
0.540	0.388(1)			
0.550		0.0564(6)		
0.560	0.310(1)			
0.580	0.2465(9)			
0.600	0.1935(9)	0.0132(3)		

Table 2.3: Squared winding number $\langle \mathbf{W}^2 \rangle$ (continued).

T/J	$L = 12$	$L = 24$	$L = 48$	$L = 96$	$L = 128$
0.339	1.475(1)	1.449(1)	1.432(1)	1.416(1)	1.416(1)
0.340	1.468(1)	1.442(1)	1.423(1)	1.411(1)	1.409(1)
0.341	1.462(1)	1.432(1)	1.414(1)	1.401(1)	1.398(1)
0.342	1.4557(9)	1.426(1)	1.409(1)	1.392(1)	1.389(1)
0.343	1.449(1)	1.417(1)	1.397(1)	1.382(1)	1.379(1)
0.344	1.443(1)	1.412(1)	1.392(1)	1.375(1)	1.370(1)
0.345	1.4368(9)	1.404(1)	1.383(1)	1.366(1)	1.363(1)
0.346	1.4295(9)	1.398(1)	1.374(1)	1.357(1)	1.350(1)

2.4 Universal jump in the helicity modulus

2.4.1 Kosterlitz renormalization group equations

The helicity modulus can be regarded as the renormalized coupling constant that appears in the Kosterlitz renormalization group equations. Furthermore, Weber and Minnhagen [44] regarded the renormalization group flow of the solution as the system size dependence of the helicity modulus. They observed that the estimated values at the critical temperature agree well with the theoretical prediction derived from this idea. In the present study, as we see below, we follow their idea but use a different method for the analysis in which not only the data at the critical temperature but also off-critical data are taken into account simultaneously.

The Kosterlitz renormalization group equations are

$$\frac{dx}{dl} = -y^2, \quad \frac{dy}{dl} = -xy. \tag{2.14}$$

Here, x and y are renormalized parameters after a renormalization operation up to the length scale $L \equiv L_0(T)e^l$ where $L_0(T)$ is some characteristic length of the order of the lattice constant and has no singularity at $T = T_{\mathrm{KT}}$. The renormalized coupling constant x is related to the helicity modulus and the squared winding number by the following equations [35]:

$$x = \frac{\pi\Upsilon}{T} - 2 = \frac{\pi}{2}\langle \mathbf{W}^2 \rangle - 2. \tag{2.15}$$

Equation (2.14) has an integral

$$\Delta(T) \equiv x^2(l) - y^2(l), \tag{2.16}$$

which does not depend on $l \equiv \log(L/L_0(T))$. As a function of T, this integral has no singularity at $T = T_{\mathrm{KT}}$. Therefore we can expand it in terms of the distance

from the critical temperature, i.e., $\Delta(K) = a(K - K_{\mathrm{KT}}) + b(K - K_{\mathrm{KT}})^2 + \cdots$ where $K \equiv J/T$. The solution of eq. (2.14) is given by

$$x(T, L) = \begin{cases} \sqrt{|\Delta|}\coth(\sqrt{|\Delta|}l) & (K > K_{\mathrm{KT}}) \\ l^{-1} & (K = K_{\mathrm{KT}}) \\ \sqrt{|\Delta|}\cot(\sqrt{|\Delta|}l) & (K < K_{\mathrm{KT}}). \end{cases} \tag{2.17}$$

This solution is a special case of the following form:

$$x(T, L) = l^{-1} f(\Delta l^2). \tag{2.18}$$

This "finite-size-scaling" form can be obtained from the ordinary one

$$x(T, L) = L^{\omega} g\left(\Delta L^{1/\nu}\right) \tag{2.19}$$

by replacing L by $l = \log(L/L_0(T))$. However, it is easy to see that eq. (2.18) cannot be made consistent with eq. (2.19) no matter what values are used for the exponents ω and ν. It should be also pointed out that even if we consider a little more general form for the ordinary finite size scaling

$$x(T, L) = L^{\omega} g\left(\xi(T)/L\right) \tag{2.20}$$

allowing $\xi(T)$ to have the correct temperature dependence, it is still impossible to cast the solution eq. (2.17) into this form.

From the solution eq. (2.17), it can be seen that the "scaling function" $f(X)$ has no singularity at X=0. The scaling function should take on the value 1 at the critical point:

$$f(X) = 1 + O(X). \tag{2.21}$$

Note also that our scaling form eq. (2.18) is consistent with Olsson's fitting function [Equations (11a-c) with (16) and (18) in Ref. [36]].

2.4.2 Finite-size-scaling around T_c

In Fig. 2.1, the squared winding number is plotted against the temperature. We can see the strong system size dependence characteristic to the KT transition especially around and above the critical temperature. Because of this large size dependence it is virtually impossible to estimate the critical temperature and the critical indices without knowing the "scaling form" that describes the system size dependence. Figure 2.2 shows the same data rescaled using eq. (2.18). The parameters K_{KT} and L_0 are chosen to minimize the cost function defined in Appendix B.

In Fig. 2.3, the contour plot of the cost function is shown. The cost function is the measure of the "badness" of the scaling plot. It is basically the deviation from the local linear approximation. In order to eliminate data out of critical region, we

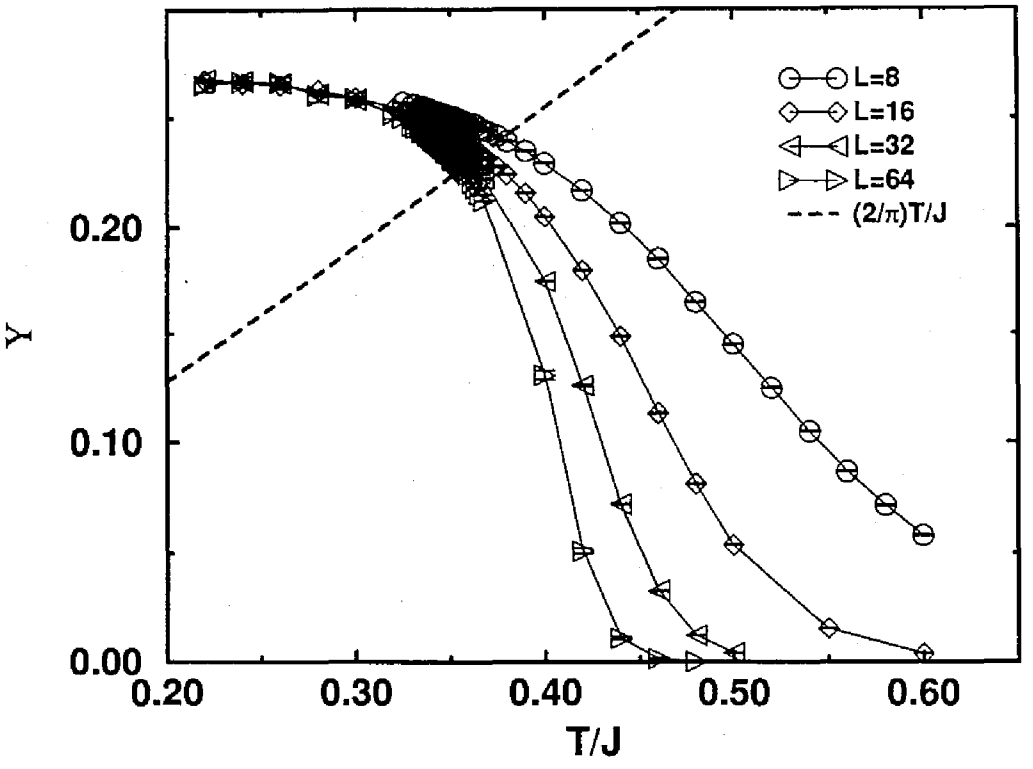

Figure 2.1: Helicity modulus (or super fluid density) $\Upsilon = (T/2)\langle \mathbf{W}^2 \rangle$ as a function of temperature. The universal jump is expected at the point where $\Upsilon = 2T/\pi$. Error bars are drown but most of them are so small that they cannot be recognized.

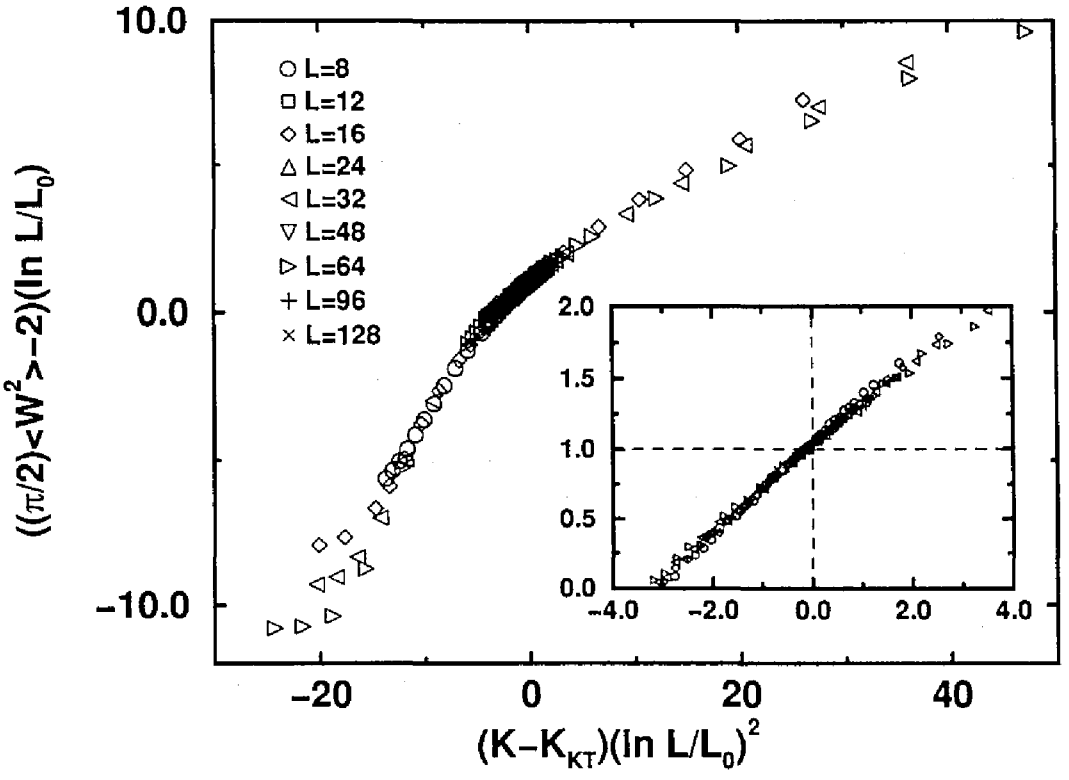

Figure 2.2: A rescaled plot of the winding number fluctuation. The inset is a enlarged view near the critical point.

have to select data points for the analysis. We have eliminated data points outside of the region,

$$\frac{4}{\pi} \leq \langle \mathbf{W}^2 \rangle \leq \frac{4}{\pi} + \frac{1}{2}, \tag{2.22}$$

$$-1.5 \leq x \equiv (K - K_{\mathrm{KT}})(\log(L/L_0))^2 \leq 1.5. \tag{2.23}$$

The value of the cost function at the optimal choice of the parameters tends to be smaller as we eliminate more data points away from the critical point, making the resulting estimate more reliable. We have also selected data points with respect to the system size. However, if we eliminate too many data points the cost function does not have a meaningful minimum. As long as we obtain a meaningful minimum, the results do not significantly depend on the minimum system size adopted, as can be seen in Fig. 2.3. For the upper contour plot in Fig. 2.3 we have used data for system size $L \geq 8$, whereas for the lower we used $L \geq 12$.

We here quote the estimates adopted in Fig. 2.2:

$$T_{\mathrm{KT}} = 0.3427(2)J, \quad L_0 = 0.29(2). \tag{2.24}$$

The minimum value of the cost function turns out to be 1.9. The deviation of this value from unity suggests the presence of correction to scaling. We can see from Fig. 2.2, that the value of the scaling function $f(x)$ at $x = 0$ is close to unity in agreement with the prediction (eq. (2.21)). The error in $f(0)$ was determined in a similar fashion to those for T_{KT} and L_0. It results in

$$f(0) = 1.0(1). \tag{2.25}$$

This agreement can hardly be explained unless the Kosterlitz–Thouless picture is assumed and is a clear indication for its validity in the present model.

2.4.3 Finite-size-scaling at T_c

We have also tried another analysis following Weber and Minnhagen [44], namely, measuring the chi-square values of the fitting to the critical form (The second equation in eq. (2.17)) as a function of the temperature. To be more specific, we assumed at each temperature the following system size dependence of the helicity modulus.

$$\frac{\pi \Upsilon}{2T} = \frac{\pi}{4}\langle \mathbf{W}^2 \rangle = A(T)\left(1 + \frac{1}{2\log(L/L_0(T))}\right) \tag{2.26}$$

This fitting form is expected to be correct only at the critical point with $A(T_{\mathrm{KT}}) = 1$ (eq. (2.18) and eq. (2.21)).

Since the number of data at each temperature is not enough, the critical temperature cannot be determined as the one at which the fitting is the best. Instead, we have tried two procedures. One is to fix $A(T)$ to be 1 (but keep L_0 as a fitting

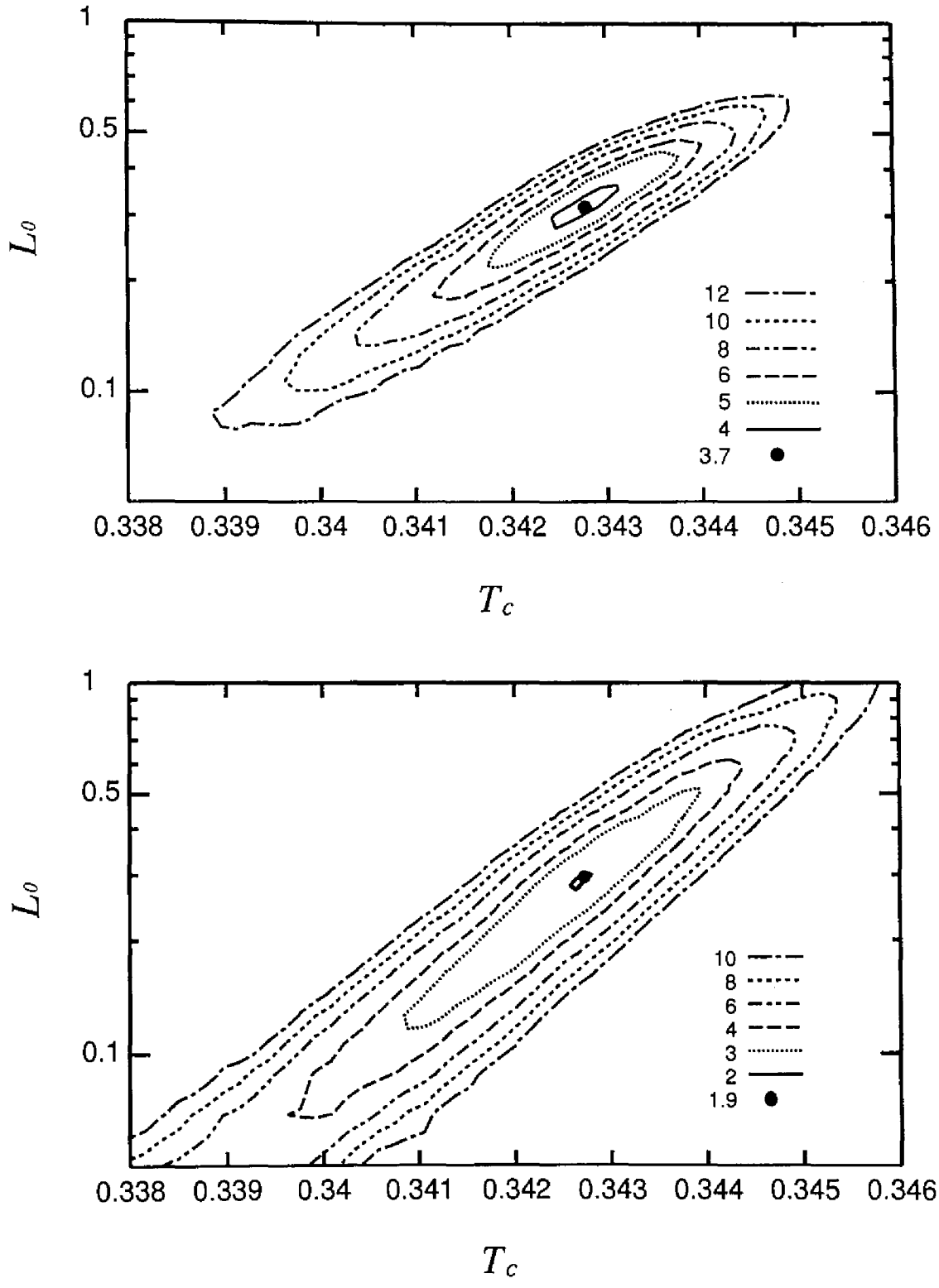

Figure 2.3: Contour plots of the cost function for evaluating finite-size-scaling plots. The plotted value is defined as S/N in Appendix B. The smallest system size used is $L = 8$ for the top figure and $L = 12$ for the bottom.

variable) and measure the chi-square values of the fitting. The result is shown in Fig. 2.4. From this figure we conclude that $T_{\rm KT} = 0.3430(5)$. The other procedure is to allow the coefficient $A(T)$ to vary and see where $A(T)$ crosses the line of $A = 1$, which should be the case at the critical temperature. The estimated coefficient $A(T)$ as a function of temperature while both A and L_0 are allowed to vary is shown in Fig. 2.5. The critical temperature is estimated by a linear fitting of the data, yielding

$$T_{\rm KT} = 0.34271(5)J, \tag{2.27}$$

which is consistent with eq. (2.24).

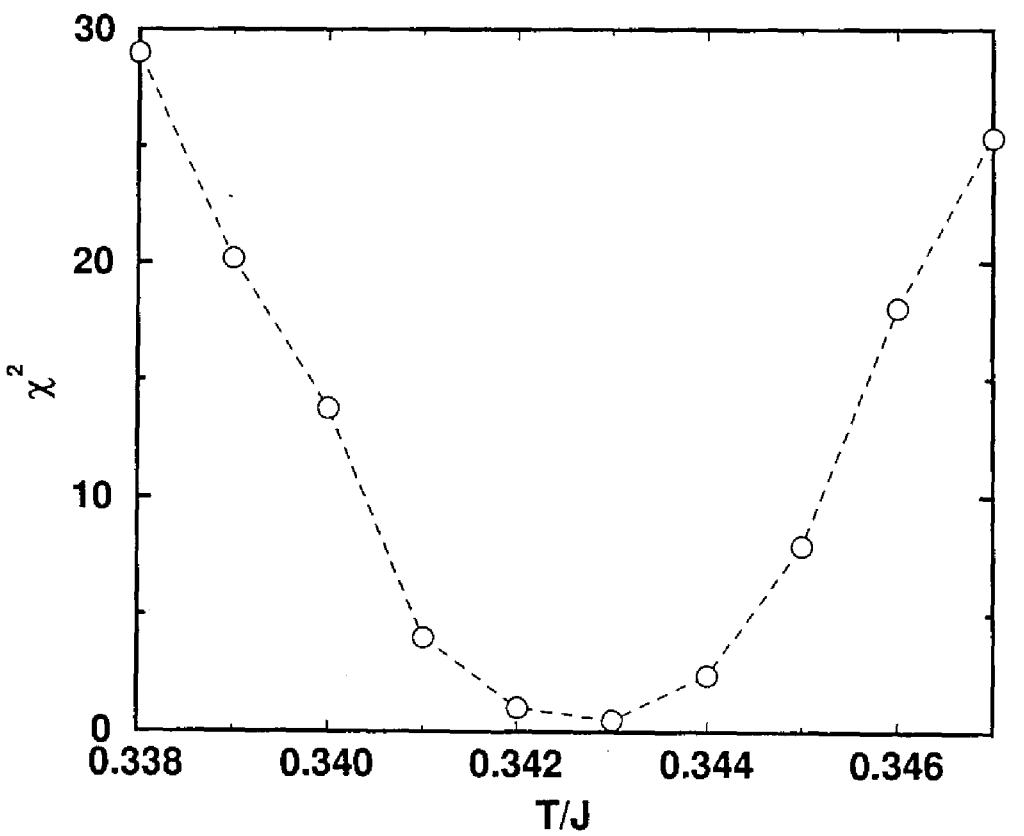

Figure 2.4: Chi-square values of the fitting with $A(T)$ fixed to be 1.

2.5 Conclusion

We have obtained accurate estimates of the helicity modulus as a function of temperature and system size. The results fit into the special finite size scaling form

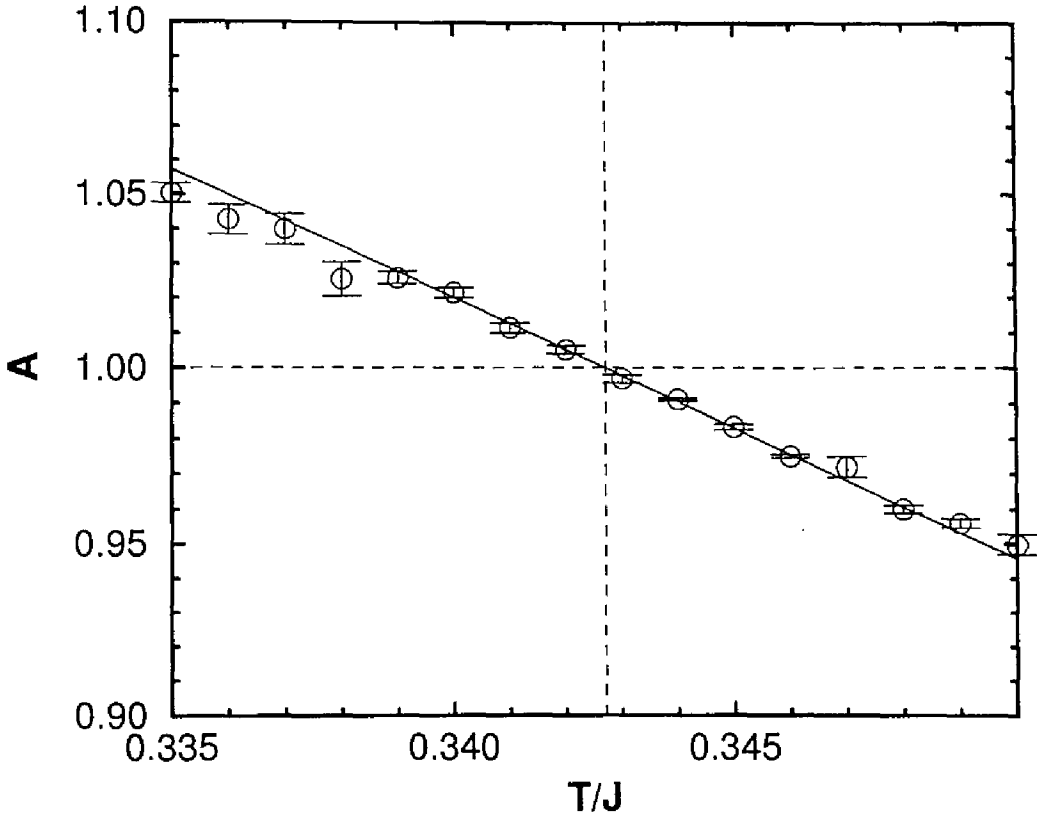

Figure 2.5: Helicity modulus divided by the magnitude of its universal jump. The dashed vertical line indicates the critical temperature at which the solid line crosses the dashed horizontal line ($A = 1$). The solid line is determined by a linear fitting.

derived from the Kosterlitz renormalization group equation identifying the renormalization scale with the system size. By this scheme we have avoided a technically difficult comparison between an exponential divergence and an algebraic one. The coincidence of the estimated critical value of the scaling function with the predicted one confirms the KT nature of the phase transition. In the numerical simulation we have used loop algorithms in both discrete and continuous time representations. Both of them have turned out to be quite efficient and advantageous especially in estimating the helicity modulus which is usually a conserved quantity in conventional Monte Carlo simulation.

3. Two dimensional $S = 1$ quantum Heisenberg antiferromagnet at finite temperatures

3.1 Introduction

Recently, field theoretical predictions [5, 6, 19] concerning the correlation length of the square lattice quantum Heisenberg antiferromagnet (QHA) were directly checked by experimental measurements [15, 34] and several quantum Monte Carlo (QMC) simulations [3, 27, 28, 32]. While in the case of spin $S = 1/2$ the validity of the predictions seemed supported by experiments, in the case of $S = 1$, experimental measurements for both La_2NiO_4 [34] and K_2NiF_4 [15] turned out to be inconsistent with the theoretical predictions.

The inconsistencies were explained by noting that the theoretical low temperature expression is valid for the temperatures of the $S = 1/2$ experiments, but not valid in the temperature regime of the $S = 1$ experiments. While a number of simulations have been performed for $S = 1/2$, only a high temperature series expansion calculation [13] and an effective high temperature theory (PQSCHA) [7–9] are available for $S = 1$ in the experimentally relevant temperature range.

In this chapter, we compute the correlation length and other thermal averages for the $S = 1$ QHA on a square lattice using the loop algorithm generalized to larger spins [23–25] and compare them with theoretical predictions and experimental measurements.

The loop algorithm was implemented on continuous imaginary time to eliminate the systematic error due to Suzuki–Trotter discretization of path integrals. We found that this algorithm was more simple and efficient for the $S = 1$ QHA than that on discrete imaginary time. The improved estimators for the $S = 1$ QHA are defined and are used to reduce the statistical error.

In Sec. 3.2 we describe the loop algorithm on continuous imaginary time for $S = 1$ QHA. In Sec. 3.3, the estimator of correlation length and improved estimators for various observables are defined and the details of simulations are explained. In Sec. 3.4 we analysis the results of quantum Monte Carlo simulations. We summarize the conclusion in Sec. 3.5.

3.2 Loop algorithm for $S = 1$ quantum Heisenberg antiferromagnet

The $S = 1$ QHA is defined by the following Hamiltonian,

$$\hat{H} = J \sum_{\langle ij \rangle} (\hat{S}_i^x \hat{S}_j^x + \hat{S}_i^y \hat{S}_j^y + \hat{S}_i^z \hat{S}_j^z), \tag{3.1}$$

where $\langle ij \rangle$ runs over all nearest-neighbor pairs on the square lattice and $\hat{S}_i^\mu$ $(\mu = x, y, z)$ is a spin-1 operator at site i.

When implemented in continuous imaginary time, the probability for the graph assignment in the cluster algorithms for larger spins becomes much simpler than the original discrete time version [23, 25], although the idea is essentially the same.

As in the case of discrete time, we first extend the Hilbert space by expressing each spin operator by a sum of $2S$ Pauli spins:

$$\hat{S}_i^\mu = \frac{1}{2} \sum_{l=1}^{2S} \hat{\sigma}_{il}^\mu, \qquad (\mu = x, y, z). \tag{3.2}$$

We therefore consider $(2SN)$ vertical lines along the imaginary time axis, each specified by two indices (il), where N is the total number of original spins. Thus a interaction term of $S = 1$ QHA is decomposed into four ones of $S = 1/2$ QHA.

For $S = 1/2$ QHA, $B(S_p)$ is 0 and $a(G_p)$ is defined in Table 3.1 (see Table 1.2 and eq. (1.47)). Although $a(2)$ is negative, it can be made positive by using a unitary

Table 3.1: $a(G_p)$ for $S = 1/2$ quantum Heisenberg antiferromagnet.

G_p	$a(G_p)$
1	$-\frac{1}{4}J$
2	$-\frac{1}{2}J$
3	0
4	0

transform as rotation $\hat{\sigma}^{x,y} \to -\hat{\sigma}^{x,y}$ on a bipartite lattice. $a(2)$ is $J/2$.

Thus our procedure for the graph assignment is simple as follows:

- For each pair of neighboring worldlines and for each uninterrupted time interval during which spins on these worldlines are antiparallel, we generate "cuts" (graph $G_p = 2$) of worldlines with probability density $J/2$.

While the loop algorithm on discrete imaginary time need more graphs as two worldlines jump at a time, this algorithm do not need them.

Since there are unphysical states in the new extend Hilbert space in which some of the spins have magnitude less than S, we must eliminate such states by applying

projection operators. Here we use a representation where z-spin components are diagonalized. The application of the projection operator for a site is realized by choosing an appropriate boundary condition in Trotter direction as follows:

- If the spin values $(\hat{\sigma}^z_{(il)}(\tau))$ are the same at the four end points, $(i1)$ and $(i2)$ at $\tau = \beta$ and at $\tau = 0$, we choose a straight connection and a cross connection with equal probability. The straight connection is to connect $(i1)$ and $(i2)$ at $\tau = \beta$ to $(i1)$ and $(i2)$ at $\tau = 0$, respectively. The cross one is to connect $(i1)$ and $(i2)$ at $\tau = \beta$ to $(i2)$ and $(i1)$ at $\tau = 0$, respectively.
- Otherwise, we choose the unique method for connecting these four points pairwise so that the spin value at each connection point is continuous.

Thus, we form many loops which are to be flipped with probability $1/2$. This algorithm turns out to be more efficient than its discrete version.

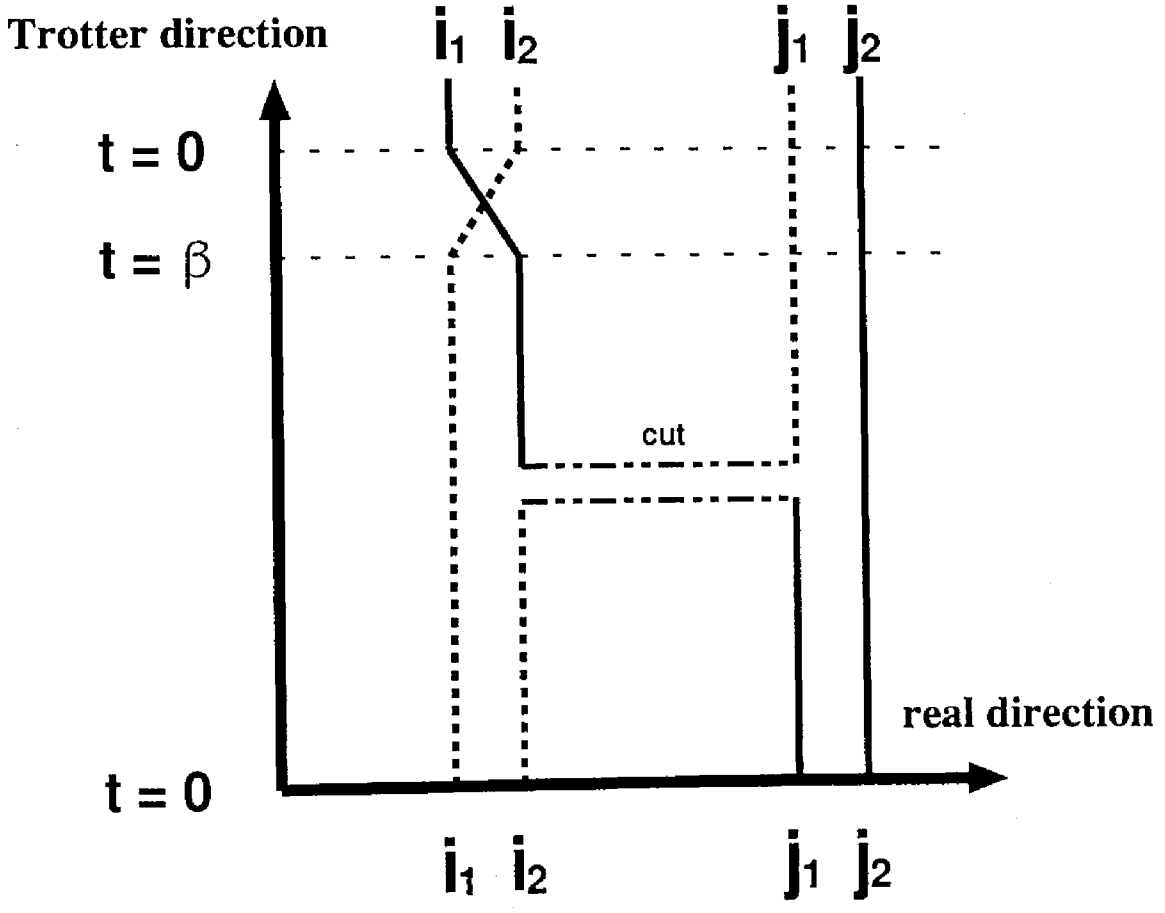

Figure 3.1: A cut and two horizontal segments. The two types of boundary condition in the Trotter direction are also illustrated.

3.3 Quantum Monte Carlo simulation

3.3.1 Estimator of correlation length

The second moment correlation length ξ_L on a finite system of size L was determined from the static structure factor $S_L(\mathbf{q})$ in the vicinity of $\mathbf{Q} = (\pi, \pi)$ [2]. The ξ_L is calculated as follows.

$$\xi_L^{-2} \equiv f(2\pi/L, 0) + f(0, 2\pi/L) - f(2\pi/L, 2\pi/L), \tag{3.3}$$

where

$$f(\mathbf{q}) \equiv 4\sin^2\left(\frac{\mathbf{q}}{2}\right)\left(1 - \frac{S(\mathbf{Q}+\mathbf{q})}{S(\mathbf{Q})}\right)^{-1}. \tag{3.4}$$

This estimator for the correlation length (of a finite system) should be correct up to the fourth order in $2\pi/L$.

3.3.2 Improved estimator

We use improved estimators to reduce statistical errors of measured quantities of the static structure factor and the uniform susceptibility.

The improved estimator of the static structure factor is defined as eq. (1.51):

$$S(\mathbf{q}) \equiv \frac{1}{V}\left(\sum_{\mathbf{r}} \exp(-i\mathbf{q}\cdot\mathbf{r}) S^z_{\mathbf{r}}(\tau)\right)^2 \tag{3.5}$$

$$= \frac{1}{4V}\left(\sum_{\mathbf{r},l} \exp(-i\mathbf{q}\cdot\mathbf{r}) \sigma^z_{\mathbf{r},l}(\tau)\right)^2, \tag{3.6}$$

$$S_{impr}(\mathbf{q}) \equiv \frac{1}{V}\sum_c (M_c(\mathbf{q}))^2, \tag{3.7}$$

where V is volume of system and c denotes a loop and $M_c(\mathbf{q})$ is

$$M_c(\mathbf{q}) \equiv \frac{1}{2}\sum_{(\mathbf{r},l)\in c} \exp(-i\mathbf{q}\cdot\mathbf{r}) \sigma^z_{\mathbf{r},l}(\tau). \tag{3.8}$$

Here we have to note that a loop is on spin-1/2 sites not on spin-1. Thus the improved estimator is defined by $\sigma^z_{\mathbf{r},l}$ not by $S^z_{\mathbf{r}}$.

Although we can use eq. (3.7) at any imaginary time τ, we have used it by several imaginary time interval $\Delta\tau$ at a certain time to reduce statistical error. In our simulation $\Delta\tau$ is 1.

The improved estimator of uniform susceptibility is simple:

$$\chi_{impr} \equiv \frac{1}{V}\sum_c \chi_c, \tag{3.9}$$

where χ_c is

$$\chi_c \equiv \left[\frac{1}{2}\sum_{(\mathbf{r},l)\in c}\sigma^z_{\mathbf{r},l}(0)\right]^2 . \tag{3.10}$$

3.3.3 Simulations

As the analytic low temperature form is not valid in the experimentally accessible temperature regime, we performed QMC simulations over the temperature range $k_BT \geq J$ in order to compare the experimental data [34] with the $S = 1$ QHA.

For a given temperature T, when the lattice size L is sufficiently large, ξ_L defined by eq. (3.3) converges to a size-independent value $\xi(T)$, which we regard as the infinite-size limit. We find that the convergence is achieved to the accuracy determined by the present statistical error when the condition $L \geq 7\xi_L$ is satisfied. All the following results are obtained under this condition. For each simulation we have performed 10^6 sweeps after 10^4 thermalization sweeps.

A selection for our results of the correlation length ξ, the staggered structure factor $S(\pi,\pi)$ and the uniform susceptibility χ are summarized in Table 3.2.

Table 3.2: Correlation length ξ, magnetic structure factor $S(\pi,\pi)$ and uniform susceptibility χ as a function of temperature $t = k_BT/2\pi\rho_s$.

J/k_BT	t	L	ξ	$S(\pi,\pi)$	χ
0.10	1.83	20	0.298(5)	0.8915(1)	0.051579(6)
0.15	1.22	20	0.396(5)	1.0489(2)	0.068503(9)
0.20	0.92	20	0.497(5)	1.2481(3)	0.08118(1)
0.25	0.73	20	0.610(5)	1.5029(5)	0.09038(1)
0.30	0.61	20	0.739(5)	1.8342(7)	0.09687(2)
0.35	0.52	20	0.894(6)	2.272(1)	0.10108(2)
0.40	0.46	20	1.079(6)	2.854(2)	0.10343(2)
0.45	0.41	20	1.307(6)	3.648(2)	0.10435(3)
0.50	0.37	30	1.604(3)	4.776(1)	0.104000(8)
0.55	0.33	30	1.982(8)	6.392(4)	0.10275(2)
0.60	0.31	40	2.482(5)	8.795(2)	0.100756(8)
0.65	0.28	40	3.14(1)	12.46(1)	0.09829(3)
0.70	0.26	50	4.06(1)	18.25(2)	0.09560(2)
0.75	0.24	50	5.30(2)	27.60(3)	0.09275(3)
0.80	0.23	60	7.06(2)	43.30(5)	0.09000(3)
0.85	0.22	80	9.52(3)	70.03(8)	0.08746(3)
0.90	0.20	120	12.98(4)	116.4(1)	0.08516(3)
0.95	0.19	140	17.97(5)	198.8(3)	0.08309(3)
1.00	0.18	200	24.94(7)	344.0(4)	0.08133(2)

3.4 Results and analysis

3.4.1 Correlation length

Using chiral perturbation theory, Hasenfratz and Niedermayer (HN) [19] obtained the temperature dependence of the correlation length up to two-loop order for an arbitrary magnitude of spin:

$$\xi_{HN} = \frac{e}{8}\frac{\hbar c}{2\pi\rho_s}\exp\left(\frac{1}{t}\right) \times \left[1 - \frac{t}{2} + \mathcal{O}\left(t^2\right)\right], \tag{3.11}$$

where $t \equiv k_B T/2\pi\rho_S$. The dependence on the magnitude of the spin S is only implicit through the S-dependence of the the spin-stiffness constant ρ_s, and the spin wave velocity c. For $S = 1/2$, the spin wave theory (SWT) [18] values for ρ_s and c were observed to be close to the QMC estimates. As SWT is better for larger spins, we can confidently use the SWT values for $S = 1$ in the following with $2\pi\rho_s = 5.461J$ and $\hbar c = 3.067J$. These values agree to within 1% with the result of a series expansion about the Ising limit.

Equation (3.11) is valid in the renormalized classical regime where

$$t \ll 1. \tag{3.12}$$

An additional constraint on the temperature comes from the cutoff of the quantum fluctuations in the effective field theory once the extension in the imaginary time direction β becomes smaller than the lattice spacing $a/\hbar c$:

$$t \ll \frac{\hbar c}{2\pi\rho_s a} \approx \frac{\sqrt{2}}{\pi}\frac{1}{S}\left(1 + \frac{0.196}{S}\right). \tag{3.13}$$

The approximation in the last term on the right hand side is again the leading order SWT result.

In the case of $S = 1/2$ QHA, it was found by QMC simulations that eq. (3.11) is valid only at very large correlation lengths [3,28] of the order of 100 lattice spacings or larger. In the experimentally relevant temperature regime the deviations, while clearly visible in the QMC simulations, are however smaller than the experimental errors. Thus, the theory and experiment agree for $S = 1/2$.

The large discrepancies observed for $S = 1$ [15,34] are somewhat counterintuitive, since the theory based on a spin-wave picture should be better for larger spins. Actually however, as noted previously in refs. 3, 5, 13, 28, larger spins are more classical. Therefore the quantum effects, which determine eq. (3.11) are cut off at lower temperatures for larger spins, as can be seen from eq. (3.13). The validity of eq. (3.11) is then restricted to even larger correlation lengths than for $S = 1/2$, much larger than accessible in experiments.

In Fig. 3.2, we plot our QMC results for the correlation length together with the experimental data [34] and theoretical predictions based on eq. (3.11). Our

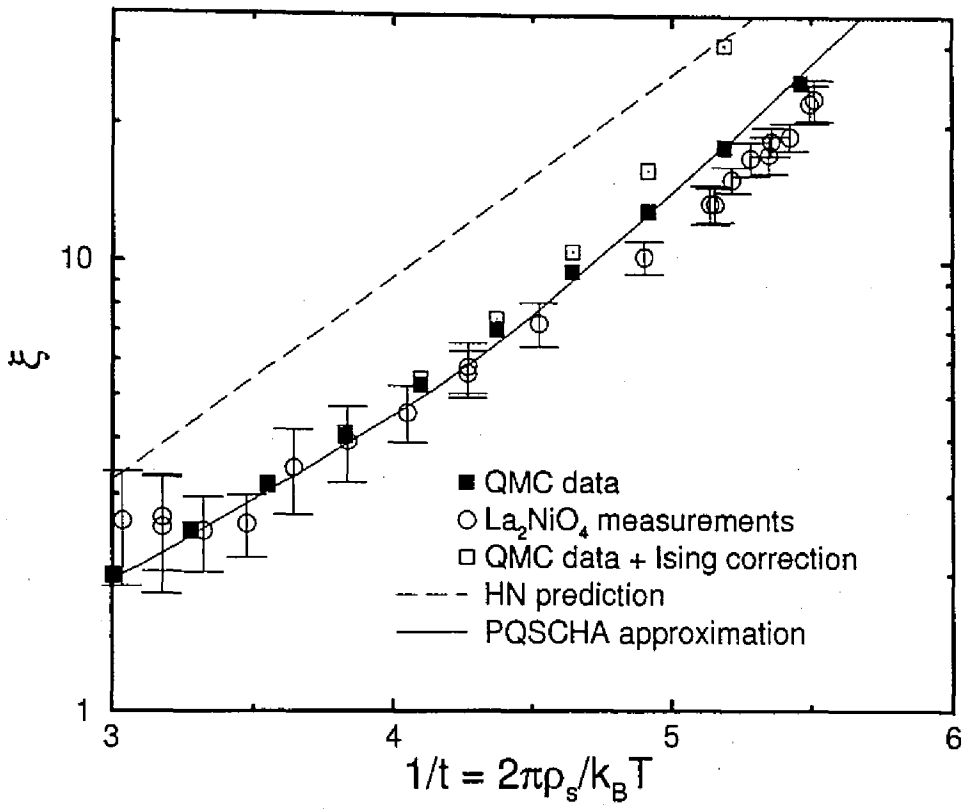

Figure 3.2: Correlation length ξ as a function of $t = k_B T/2\pi\rho_s$. Filled squares represent the results of our simulation, the open circles are experimental measurements [34]. While the experimental measurements agree roughly with our QMC results, they are incompatible with the QMC results corrected for a small Ising anisotropy (open squares). Compared to analytic calculations, we find that in this temperature range the low-temperature predictions of eq. (3.11) (dashed line) are not valid. The PQSCHA approximation [7–9], however agrees well with both our data and the experimental measurements.

present estimates are in rough agreement with experimental measurements. Greven *et al.* [15] and Nakajima *et al.* [34] have additionally proposed to include the effects of a small Ising anisotropy using a mean-field type correction to the theoretical isotropic results. This correction (eq.(7) in ref. 34) however makes the agreement worse, as can be seen from Fig. 3.2.

Compared to theoretical predictions we find that the data deviate strongly from the low temperature formula of eq. (3.11). The effective PQSCHA approximation [7–9], which is an effective high temperature theory, however agrees well with the QMC results much better than for $S = 1/2$ [7–9,27].

3.4.2 Structure factor

The violation of the theoretical predictions [5,6] was observed in the peak value of the staggered structure factor $S(\pi,\pi)$, which according to the theory [5,6] should scale as

$$S(\pi,\pi) = A2\pi M^2\xi^2t^2(1+Ct). \tag{3.14}$$

Here M is the staggered magnetization of the ground state and A and C are universal constants. For spin-1/2 the leading t^2 form was confirmed by high temperature series [13]. Recent QMC data [28] at lower temperatures fit the above form very well in the temperature range $t < 3$ with $A \approx 4.0(1)$ and $C \approx 0.5(1)$. However, experiments for both $S = 1/2$ and $S = 1$ however were better described by an empirical law [15,34]

$$S(\pi,\pi) \propto \xi^2 \tag{3.15}$$

over the same temperature range.

We applied χ^2 analysis to check the consistency of the spin-1 data. Good fits were obtained for $t < 0.28$, with $\chi^2 \sim 1$ when we allow C to vary, and $\chi^2 \sim 2$ with a fixed $C = 0.5$. The universal constant A was determined to be $A = 4.1(1)$ and $A = 4.5(1)$, similar to the values obtained for $S = 1/2$. The discrepancies between the fits are non-universal effects caused by the high temperatures.

Compared of our data with the experiments is shown in Fig. 3.3 and we can see that for low temperatures the experimental data are consistent with the QMC results and eq. (3.14). The discrepancies that lead refs. 34 and 15 to predict eq. (3.15) occur at higher temperatures where the experimental data has large error bars. In view of the precision of our QMC results and the large errors of the experimental results we suspect that, contrary to the suggestion of refs. 34 and 15, the deviations from eq. (3.14) are due to uncertainties in the experimental measurements.

3.4.3 Uniform susceptibility

We present in Fig. 3.4 the uniform susceptibility for $S = 1/2$ together with previously published $S = 1/2$ results. First we note that, as expected, the asymptotic low

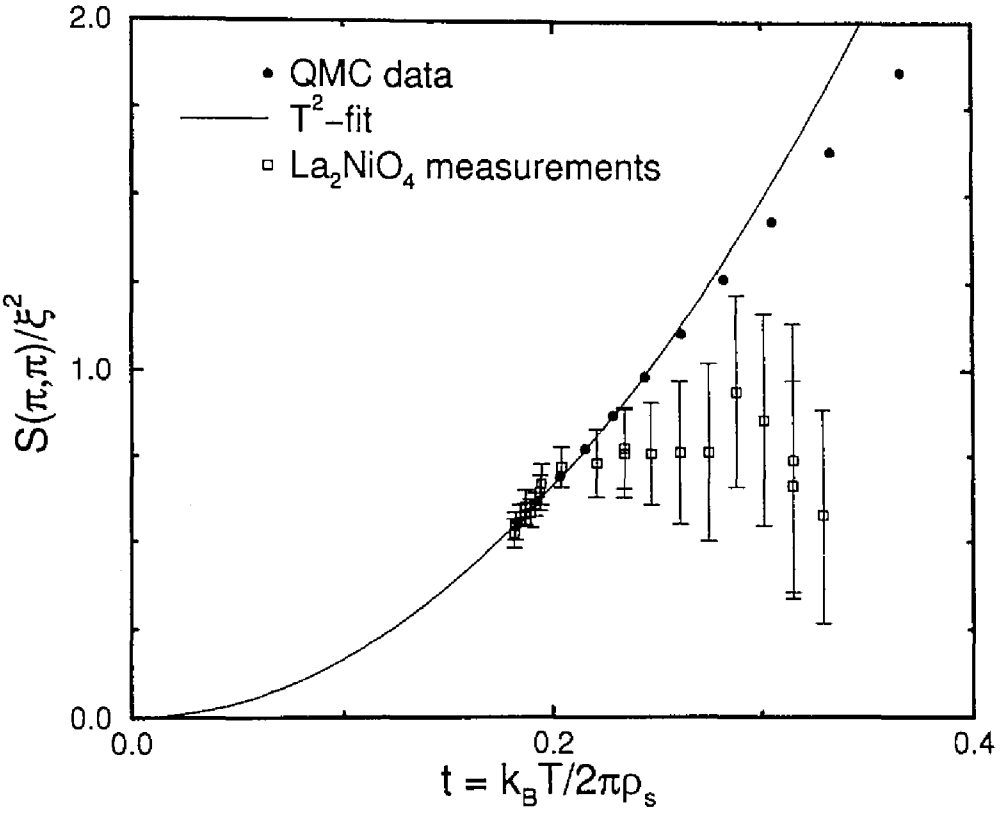

Figure 3.3: Ratio of structure factor peak value and square of the correlation length $S(\pi,\pi)/\xi^2$ as a function of temperature. Solid circles represent the QMC measurements and open squares the experimental measurements. They agree at low temperatures, but differ at higher temperatures. The solid line is a fit of the QMC data to the theoretical low-temperature prediction.

temperature behavior of the renormalized classical regime

$$\chi = \frac{2\rho_s}{3}\left(\frac{g\mu_B}{\hbar c}\right)^2 (1 + t + t^2) \tag{3.16}$$

sets in at lower temperatures for $S = 1$ than for $S = 1/2$.

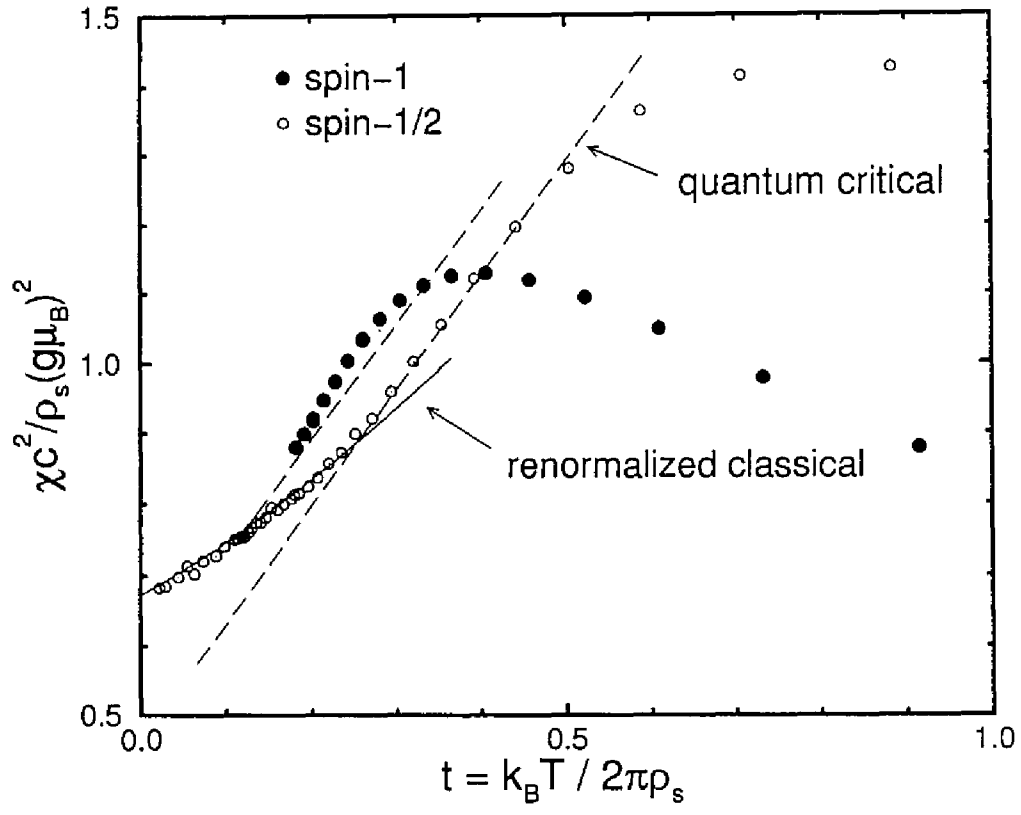

Figure 3.4: Uniform susceptibility χ as a function of temperature t for both spin $S = 1$ and spin $S = 1/2$ (taken from ref. 28). The solid line is the predicted low temperature form of the renormalized classical regime. The dashed lines have the universal slope expected for the quantum critical regime. As expected, contrary to $S = 1/2$, no extended quantum critical regime exists for $S = 1$. However the slope is close to the quantum critical value as non-universal corrections are still small for $S = 1$.

It was discovered that for $S = 1/2$, the uniform susceptibility is the only quantity for which a clear crossover to quantum critical behavior [6] can be observed at intermediate temperatures $t \sim 1/3$. The uniform susceptibility in the quantum

critical regime is

$$\chi = \chi_\perp + BT\left(\frac{g\mu_B}{\hbar c}\right)^2, \tag{3.17}$$

with a universal slope $B \approx 0.26(1)$ [6,42,43]. For $S = 1$ however, as discussed above, non-universal corrections become important at lower temperatures. No quantum critical behavior was thus expected for $S = 1$. We can see in Fig. 3.4 that the uniform susceptibility for $S = 1$ deviates from its universal quantum critical behavior at intermediate temperatures. Its slope is however still surprisingly close to the quantum critical one, indicating that the non-universal corrections are still not very large for $S = 1$.

3.5 Conclusion

We have simulated the spin $S = 1$ quantum Heisenberg antiferromagnet on a square lattice in the experimentally relevant temperature regime $k_B T \sim J$.

In the case of higher spin, the loop algorithm on continuous imaginary time is also more effective and efficient than the traditional worldline algorithms [32] and simpler than on discrete imaginary time. Improved estimators have worked well and are simple to calculate.

We find a better agreement between the Heisenberg model and experimental data than is expected from the low temperature theory. However, in view of the existing small discrepancies, it may be necessary to perform simulations on a model with small anisotropies in the exchange interactions, and to critically check the data analysis of the experiments.

Summary

In the present thesis, we made the best use of loop algorithms in order to investigate the spin-1/2 quantum XY model (QXY) and the spin-1 Heisenberg antiferromagnet (QHA) on the two-dimensional square lattice and have obtained the following results.

The helicity modulus in QXY is precisely estimated for systems up to 128×128 near and below the critical temperature. The critical temperature is estimated as $T_{\mathrm{KT}} = 0.3427(2)J$. The obtained estimates for the helicity modulus are well fitted by a scaling form derived from the Kosterlitz renormalization group equation. The validity of the Kosterlitz–Thouless theory for this model is confirmed.

For QHA model, the temperature dependence of the correlation length, susceptibilities and the magnetic structure factor are computed by extensive Monte Carlo simulations (QMC). In the experimentally relevant temperature regime the theoretically predicted asymptotic low temperature behavior is found to be not valid. The QMC results, however, agree reasonably well with the experimental measurements of La_2NiO_4 even without considering anisotropies in the exchange interactions.

In both QXY and QHA cases, we have found that loop algorithms are very effective and the improved estimators work well as expected. Consequently, it can be said that the loop algorithm is the best tool for numerical studies for quantum spin models at low temperatures and critical points.

A. Markov chain approach

In order to make a sequence of configurations on the desired distribution in Monte Carlo simulations, we usually use a Markov chain. A configuration S_{now} in a Markov chain is made from a previous configuration S_{prev} by a transition probability $P(S_{prev} \to S_{now})$.

When the transition probability satisfies the following conditions:

$$P(S)P(S \to S') = P(S')P(S' \to S) \tag{A.1}$$

and

$$P(S \to S') > 0 \qquad (P(S') > 0), \tag{A.2}$$

then the appearance probability of a configuration S on the Markov chain converges the distribution $P(S)$. It is useful in Monte Carlo simulations. Equation (A.1) and (A.2) are called the detailed balance condition and the ergodicity condition, respectively. The transition probability used in Monte Carlo simulations needs to satisfy these conditions.

There are two popular transition probabilities:

Metropolis' method

$$P(S \to S') \equiv \min(1, P(S')/P(S)), \tag{A.3}$$

Heat-bath method

$$P(S \to S') \equiv \frac{P(S')}{P(S) + P(S')}. \tag{A.4}$$

Almost local update Monte Carlo methods use these transition probabilities.

B. Cost function for evaluating finite-size-scaling plots

In this appendix, we present a new estimator for evaluating finite-size-scaling plots. The estimator is basically a deviation from a local linear approximation analogous to the previous estimator [26]. The advantage of this type of approaches is that we do not need to assume any specific functional form for the scaling function. These estimators are functions of trial values for various parameters such as critical indices and temperature; $K_{\rm KT}$ and L_0 in the case of quantum XY model (QXY). Since the previous estimator was discontinuous as a function of these parameters, searching for its minimum — the optimal point — was a rather tricky task. One could hardly tell if a local minimum found was really a global minimum. The discontinuity came from the reordering of the data points as we change the trial values of the exponents and the critical temperature. As we show in the following, we have eliminated this discontinuity by treating data points for different system size separately.

In what follows, a data point consists of a rescaled estimate y, a rescaled error d and a rescaled parameter x at which y and d are estimated. In the case of QXY, $y = ((\pi/2)\langle W^2\rangle - 2)\log(L/L_0)$ and $x = (K - K_{\rm KT})(\log(L/L_0))^2$. Therefore, x, y and d depend on trial values for various parameters in general. Here we denote one standard deviation by d. Also we denote the i-th data point for the system size L by $P_{L,i} \equiv (x_{L,i}, y_{L,i}, d_{L,i})$. These data points are ordered so that $x_{L,i} < x_{L,i+1}$. In the previous estimator, we dealt with all the data points without regard to the system size. Therefore, the order of the data points may change as the trial values for the exponents vary. Here we have no such reordering due to the change in the trial values.

For each system size L', we connect adjacent points $P_{L',i}$ and $P_{L',i+1}$ by a straight line. Then, for each combination of a data point $P_{L,i}$ and a system size L', we choose j such that $x_{L',j} < x_{L,i} < x_{L',j+1}$. Next, we consider a point at $x = x_{L,i}$ on the line that connects two points, $P_{L',j}$ and $P_{L',j+1}$. We denote this point by $P^{L'}_{L,i}$. Since the value $y^{L'}_{L,i}$ is expressed as a linear combination of $y_{L',j}$ and $y_{L',j+1}$,

$$y^{L'}_{L,i} \equiv p y_{L',j} + q y_{L',j+1}, \tag{B.1}$$

$$p \equiv \frac{x_{L',j+1} - x_{L,i}}{x_{L',j+1} - x_{L',j}}, \quad q \equiv 1 - p, \tag{B.2}$$

the error $d^{L'}_{L,i}$, which comes from errors $d_{L',j}$ and $d_{L',j+1}$, can be estimated through

the ordinary error propagation rule. To be specific,

$$d_{L,i}^{L'} = \sqrt{p^2 d_{L',j}^2 + q^2 d_{L',j+1}^2}. \tag{B.3}$$

For convenience, we define $P_{L,i}^{L} \equiv P_{L,i}$. In an ideal case where the linear approximation is good and the statistical and systematic errors are negligible, all $P_{L,i}^{L'}$'s for various L' should coincide with each other.

Here we assume that the linear approximation is good and the systematic errors are negligible while the statistical errors are not necessarily negligible. In order to evaluate the coincidence, then, we consider the weighted sum of deviations of the points $P_{L,i}^{L'}$, i.e.,

$$S_{L,i} \equiv \sum_{L'} \frac{1}{n-1} \left(\frac{y_{L,i}^{L'} - \bar{y}_{L,i}}{d_{L,i}^{L'}} \right)^2 \tag{B.4}$$

with

$$\bar{y}_{L,i} \equiv \sum_{L'} \frac{y_{L,i}^{L'}}{d_{L,i}^{L'\,2}} \Bigg/ \sum_{L'} \frac{1}{d_{L,i}^{L'\,2}}, \tag{B.5}$$

where n is the number of distinct system sizes. As statistics tells, the expectation value of $S_{L,i}$ is 1. When we define S as the sum of all $S_{L,i}$'s, it evaluates quality of the finite-size-scaling plot. Its expectation value equals the number of data points N. The acceptable range of parameters is determined by

$$S < \min S + m, \tag{B.6}$$

where m is of order O(1).

References

[1] A. V. Aho, J. E. Hopcroft and J. D. Ullman, *The Design and Analysis of Computer Algorithms*, (Addison-Wesley, 1974).

[2] G. A. Baker, Jr. and N. Kawashima, Phys. Rev. Lett. **75**, 994 (1995).

[3] B. B. Beard, R. J. Birgeneau, M. Greven and U.-J. Wiese, Phys. Rev. Lett. **80**, 1742 (1998).

[4] B. B. Beard and U. J. Wiese, Phys. Rev. Lett. **77**, 5130 (1996).

[5] S. Chakravarty, B. I. Halperin and D. R. Nelson, Phys. Rev. B **39**, 2344 (1989).

[6] A. V. Chubukov, S. Sachdev and J. Ye, Phys. Rev. B **49**, 11919 (1994).

[7] A. Cuccoli, V. Tognetti, R. Vaia and P. Verrucchi, Phys. Rev. Lett. **77**, 3439 (1996).

[8] A. Cuccoli, V. Tognetti, R. Vaia and P. Verrucchi, Phys. Rev. Lett. **79**, 1584 (1997).

[9] A. Cuccoli, V. Tognetti, R. Vaia and P. Verrucchi, Phys. Rev. B **56**, 14456 (1997).

[10] H.-Q. Ding, Phys. Rev. B **45**, 230 (1992).

[11] H.-Q. Ding and M. S. Makivić, Phys. Rev. B **45**, 491 (1992).

[12] H.-Q. Ding and M. S. Makivić, Phys. Rev. B **42**, 6827 (1990).

[13] N. Elstner, A. Sokol, R. R. P. Singh, M. Greven and R. J. Birgeneau, Phys. Rev. Lett. **75**, 938 (1995).

[14] H. G. Evertz, M. Marcu and G. Lana, Phys. Rev. Lett. **70**, 875 (1993).

[15] M. Greven, R. J. Birgeneau, Y. Endoh, M. A. Kastner, M. Matsuda and G. Shirane, Z. Phys. B **96**, 465 (1995).

[16] R. Gupta, J. DeLapp, G. G. Batrouni, G. C. Fox, C. F. Baillie and J. Apostolakis, Phys. Rev. Lett. **61**, 1996 (1988).

[17] R. Gupta and C. F. Baillie, Phys. Rev. B **45**, 2883 (1992).

[18] C. J. Hammer, Z. Weihong and J. Oitmaa, Phys. Rev. B **50**, 6877 (1994).

[19] P. Hasenfratz and F. Niedermayer, Phys. Lett. B **268**, 231 (1991).

[20] D. Kandel and E. Domany, Phys. Rev. B **43**, 8539 (1991).

[21] P. W. Kasteleyn and C. M. Fortuin, J. Phys. Soc. Jpn. **26**(Suppl.), 11 (1969).

[22] C. M. Fortuin and P. W. Kasteleyn, Physica **57**, 536 (1972).

[23] N. Kawashima, J. Stat. Phys. **82**, 131 (1996).

[24] N. Kawashima and J. E. Gubernatis, Phys. Rev. Lett. **73**, 1295 (1994).

[25] N. Kawashima and J. E. Gubernatis, J. Stat. Phys. **80**, 169 (1995).

[26] N. Kawashima and N. Ito, J. Phys. Soc. Jpn. **62**, 435 (1993).

[27] J.-K. Kim, D. P. Landau and M. Troyer, Phys. Rev. Lett. **79**, 1583 (1997).

[28] J.-K. Kim and M. Troyer, Phys. Rev. Lett. **80** (1998) in press.

[29] J. M. Kosterlitz, J. Phys. C **7**, 1046 (1974).

[30] J. M. Kosterlitz and D. J. Thouless, J. Phys. C **6**, 1181 (1973).

[31] M. S. Makivić, Phys. Rev. B **46**, 3167 (1992).

[32] M. S. Makivić and H.-Q. Ding, Phys. Rev. B **43**, 3562 (1991).

[33] H. Mino, Comp. Phys. Comm. **66**, 25 (1991).

[34] K. Nakajima, K. Yamada, S. Hosoya, Y. Endoh, M. Greven and R. J. Birgeneau, Z. Phys. B **96**, 479 (1995).

[35] D. R. Nelson and J. M. Kosterlitz, Phys. Rev. Lett. **39**, 1201 (1977).

[36] P. Olsson, Phys. Rev. B **52**, 4526 (1995).

[37] E. L. Pollock and D. M. Ceperley, Phys. Rev. B **36**, 8343 (1987).

[38] J. Sólyom and T. A. L. Ziman, Phys. Rev. B **30**, 3980 (1984).

[39] M. Suzuki, Prog. Theor. Phys. **56**, 1454 (1976).

[40] R. H. Swendsen and J. S. Wang, Phys. Rev. Lett. **58**, 86 (1987).

[41] J. Sznajd, Phys. Rev. B **45**, 489 (1992).

[42] M. Troyer, M. Imada and K. Ueda, J. Phys. Soc. Jpn. **66**, 2957 (1997).

[43] M. Troyer and M. Imada, *Computer Simulations in Condensed Matter Physics X*, ed. D. P. Landau *et al.*, (Springer Verlag, Heidelberg, 1997).

[44] H. Weber and P. Minnhagen, Phys. Rev. B **37**, 5986 (1987).